Investigations of the thermodynamic potential at inhomogeneous phases in the Nambu-Jona-Lasinio model

Untersuchungen des thermodynamischen Potentials in inhomogenen Phasen im Nambu-Jona-Lasinio Modell
Master thesis by Carsten Wandschura
Date of submission: 29.09.2020

1. Review: Priv.-Doz. Dr. Michael Buballa
2. Review: Prof. Ph.D. Guy Moore
Darmstadt

TECHNISCHE
UNIVERSITÄT
DARMSTADT

Physics Department
Institute for nuclear physics
AG Buballa

Erklärung zur Abschlussarbeit
gemäß §22 Abs. 7 und §23 Abs. 7 APB der TU Darmstadt

Hiermit versichere ich, Carsten Wandschura, die vorliegende Masterarbeit ohne Hilfe Dritter und nur mit den angegebenen Quellen und Hilfsmitteln angefertigt zu haben. Alle Stellen, die Quellen entnommen wurden, sind als solche kenntlich gemacht worden. Diese Arbeit hat in gleicher oder ähnlicher Form noch keiner Prüfungsbehörde vorgelegen.

Mir ist bekannt, dass im Fall eines Plagiats (§38 Abs. 2 APB) ein Täuschungsversuch vorliegt, der dazu führt, dass die Arbeit mit 5,0 bewertet und damit ein Prüfungsversuch verbraucht wird. Abschlussarbeiten dürfen nur einmal wiederholt werden.

Bei der abgegebenen Thesis stimmen die schriftliche und die zur Archivierung eingereichte elektronische Fassung gemäß §23 Abs. 7 APB überein.

Bei einer Thesis des Fachbereichs Architektur entspricht die eingereichte elektronische Fassung dem vorgestellten Modell und den vorgelegten Plänen.

Darmstadt, 29.09.2020   _____

                                                                        Carsten Wandschura

Abstract

In this thesis, inhomogeneous phases with vanishing and finite current quark mass in the Nambu-Jona-Lasino model are investigated. We consider space-dependent condensates in one dimension with included vector interaction, by using finite Fourier expansions. The solutions in the thermodynamic equilibrium are derived by using minimization routines. We investigate the thermodynamic potential in the space of the relevant Fourier coefficients in the chiral limit for several vector interaction strengths to get a deeper understanding of the findings of previous works. Ensuing, we study the influence of the vector interactions on inhomogeneous phases in the presence of explicitly chiral-symmetry breaking terms.

Zusammenfassung

In dieser Thesis werden inhomogene Phasen mit verschwindender und endlicher Stromquarkmasse im Nambu-Jona-Lasinio Modell untersucht. Unter Einbeziehung von Vektorwechselwirkungen werden Fourierentwicklungen für eindimensional ortsabhängige Kondensate verwendet. Die Lösungen im thermodynamischen Gleichgewicht werden mittels Minimierungsroutinen berechnet. Um ein tieferes Verständnis für die Ergebnisse aus früheren Arbeiten zu bekommen, wird das thermodynamische Potential im chiralen Limes für verschiedene Vektorwechselwirkungen im Raum der relevanten Fourierkoeffizienten untersucht. Darauffolgend wird der Einfluss der Vektorwechselwirkungen auf inhomogene Phasen in Anwesenheit explizit chiral symmetriebrechender Terme untersucht.

Contents

1. Introduction

Figure 1.1 shows an educated guess of the phase diagram of quantum chromodynamics (QCD). It is subject to theoretical and experimental research until now [1–5]. The phase diagram describes the different states of QCD matter. It can be divided roughly into four regions [3]. At low chemical potential and temperature, the quarks are confined to hadrons (hadronic phase) and the chiral symmetry is broken. By increasing the temperature for fixed chemical potentials, a crossover transition from the confined to the deconfined phase occurs, where the quarks and gluons appear as a quark-gluon plasma (QGP) and the chiral symmetry is restored [4]. In the high density and intermediate temperature regime, a rich phase structure is expected which is called color superconducting phase [5]. For low temperatures and intermediate densities, inhomogeneous phases with crystalline structures are suggested, characterized by a spatial dependence of the system properties [6]. While most regions of the diagram remain still unknown the high temperature and low-density regime is explored by lattice QCD and heavy ion collisions. Lattice QCD is limited to a zero chemical potential. For non-vanishing chemical potential the 'sign problem' lets the method fail [7] and it is necessary to use methods like Dyson-Schwinger equations (DSE) [8–10], functional renormalization group (FRG) [11–13] or effective models, e.g. Nambu-Jona-Lasinio model (NJL model) [14, 15] or the quark-meson model [16, 17], which share important properties with the QCD.
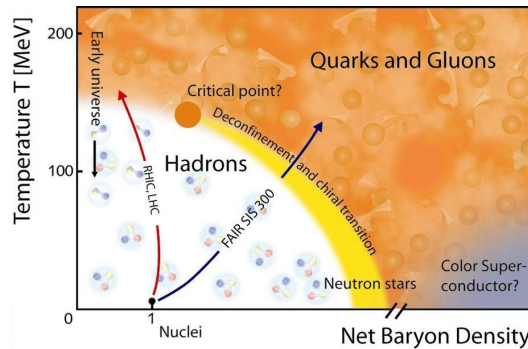
Figure 1.1.: The QCD phase diagram, taken from [18].

In 1960 Overhauser introduced the idea of inhomogeneous ground states for nuclear matter as large static density waves [19]. Fulde and Ferrell investigated inhomogeneous phases in the solid-state physics with a single plane wave in 1964 [20] and Larkin and Ochinnikov discussed them with sinusoidal modulations in the same year [21].
In this thesis inhomogeneous phases are studied in the NJL model. We extend it by vector interactions and apply the mean-field approximation. It is built on the results of the master's theses of Eduard Alert [22] and Marco Schramm [23] as well as the work of Stefano Carignano, Dominik Nickel and Michael Buballa [24]. Alert investigated the properties of the NJL model in the chiral limit as well as for explicitly broken chiral symmetry. Carignano, Nickel and Buballa studied chiral inhomogeneous phases with a constant

vector condensate and Schramm included space-depending vector condensates. In the inhomogeneous phases, a chiral density wave (CDW) was considered, which is a complex modulation for the effective mass and several real ansätze such as a sinusoidal ansatz or Fourier expansions with higher coefficients. The CDW and sinusoidal ansätze have already been investigated in detail in the NJL model without vector interactions, e.g. [6, 25], where the CDW emerged as being a self-consistent but least favored solution. A rising number of coefficients led to a gain in free energy. Thereby, all even coefficients vanished. In the chiral limit without vector interactions, the most favored solution so far is the so-called solitonic solution or 'real kink crystal' [26, 27]. They are described by the Jacobi-elliptic functions. Breaking the chiral symmetry explicitly delivered partially different results, the CDW turned out to be not self-consistent anymore and all real mass-ansätze resulted in exhibiting a constant shift that vanishes in the chiral limit. Furthermore, the even Fourier coefficients had a non-vanishing contribution.

Extending the NJL model by vector condensates at homogeneous phases led to an effective shift of the chemical potential. At inhomogeneous phases, the effective chemical potential becomes inhomogeneous which is much harder to deal with. As a first approach, in [24] the shifted chemical potential was considered as being constant. This approach is called 'average density approximation' (ADA) since it implies a homogeneous density. In [23] and [28], additionally, the shifted chemical potential was extended by a cosine which gave rise to a density amplitude. For the CDW the ADA turned out to be self-consistent. This was consistent since the CDW is known to have a homogeneous density. In contrast, the sinusoidal mass ansatz yielded a non-vanishing density amplitude. The inclusion of explicitly modulated densities had a significant effect on the phase diagram but also revealed contradictions between the two works. In [23], for vector-coupling strengths above a certain value, the CDW solution turned out to be energetically more favored compared to the sinusoidal modulation with space-depending density. Consequently, there was a border at a certain coupling strength where both solutions coexist. But Ginzburg-Landau (GL) analyses in [28] showed that the CDW is already favored for arbitrary small vector-coupling strengths in the proximity of the Lifshitz point (LP).

In this work, the aim is to get a better understanding of the stated results by investigating the thermodynamic potential with and without space-dependent vector interactions in the chiral limit. Furthermore, we will investigate the consequences of the vector interactions on inhomogeneous phases in the presence of explicitly chiral-symmetry breaking terms.

2. Nambu-Jona-Lasinio model

The Nambu-Jona-Lasinio (NJL) model [14, 15] came up in 1961, before the introduction of QCD and the existence of quark models. The model provided a field-theoretical description of nucleons, which included a mechanism for dynamical mass generation in analogy with the gap-energy in the microscopic theory of superconductivity. Later the fermionic fields in the Lagrangian have been reinterpreted as quarks. This incorporates additional quantum numbers, such as color degrees of freedom. The NJL model shares global symmetries of QCD but contains no gluons and confinement. Instead, the quark interaction is described by four-point vertices. Therefore, the model is not renormalizable and needs to be regularized.
We extend the standard two-flavor NJL-Lagrangian to describe vector interactions. Thus, the Lagrangian reads:

$$\mathcal{L}_{\mathrm{NJL}} = \underbrace{\bar{\psi}(i\gamma^\mu\partial_\mu - m)\psi}_{\equiv \mathcal{L}_{\mathrm{free}}} + \underbrace{g_s\left[(\bar{\psi}\psi)^2 + (\bar{\psi}i\gamma_5\vec{\tau}\psi)^2\right] - g_v(\bar{\psi}\gamma^\mu\psi)^2}_{\equiv \mathcal{L}_{\mathrm{int}}} \tag{2.1}$$

where $\mathcal{L}_{\mathrm{free}}$ is the free Dirac part and $\mathcal{L}_{\mathrm{int}}$ describes the four-point interactions. ψ are the two-flavor and three-color quark fields, γ are the Dirac matrices, τ the Pauli matrices acting on the two-dimensional isospin space and m is the current quark mass. Here the up- and down quark masses are assumed to fulfill $m_u = m_d$ (isospin limit). The interaction term contains a scalar ($\bar{\psi}\psi$) and pseudoscalar ($\bar{\psi}i\gamma_5\vec{\tau}\psi$) interaction term, which are characterized by the same coupling constant g_s and describe an attractive interaction. The vector interaction term with coupling constant g_v gives rise to a repulsive interaction. The standard form of the NJL-Lagrangian can be obtained by setting $g_v = 0$.

Symmetries

The symmetries of the Lagrangian lead to conservation laws by the Noether Theorem. The global phase transformation $U_V(1)$

$$\psi \to \exp(-i\alpha)\psi \ \text{ and } \ \bar{\psi} \to \exp(i\alpha)\bar{\psi} \ \text{ with } \ \alpha \in \mathbb{R} \tag{2.2}$$

gives rise to baryon number conservation. In the isospin limit, where the masses of the up- and down quarks are assumed to fulfill $m_u = m_d$, the Lagrangian is invariant under $SU_V(2)$ symmetry

$$\psi \to \exp\left(-\frac{i}{2}\vec{\tau}\cdot\vec{\omega}\right)\psi \ \text{ and } \ \bar{\psi} \to \bar{\psi}\exp\left(\frac{i}{2}\vec{\tau}\cdot\vec{\omega}\right) \ \text{ with } \ \vec{\omega} \in \mathbb{R}^3 \tag{2.3}$$

which corresponds to a rotation in isospin space. For a vanishing quark mass (chiral limit) the Lagrangian is invariant under the axial symmetry $SU_A(2)$

$$\psi \to \exp\left(-\frac{i}{2}\gamma_5\vec{\tau}\cdot\vec{\theta}\right)\psi \ \text{ and } \ \bar{\psi} \to \bar{\psi}\exp\left(-\frac{i}{2}\gamma_5\vec{\tau}\cdot\vec{\theta}\right) \ \text{ with } \ \vec{\theta} \in \mathbb{R}^3. \tag{2.4}$$

The combination $SU_V(2) \otimes SU_A(2)$ is called chiral symmetry and is only fulfilled for a vanishing current mass m. The chiral symmetry is spontaneously broken by non-vanishing condensates. So in the chiral limit, the quark condensate is an order parameter for chiral symmetry breaking. In this thesis the chiral limit, $m = 0$, as well as explicitly broken chiral symmetry, $m \neq 0$, will be considered.

2.0.1. Mean-Field Approximation

To calculate thermodynamic properties, the mean-field approximation (or equivalently Hartree) will be applied [29]. We label the expectation values of the field bilinears as

$$\phi_S(\underset{\sim}{\mathbf{x}}) \equiv \langle \bar{\psi}\psi \rangle \tag{2.5}$$

$$\phi_P^a(\underset{\sim}{\mathbf{x}}) \equiv \langle \bar{\psi}i\gamma_5\tau^a\psi \rangle \tag{2.6}$$

$$n^\mu(\underset{\sim}{\mathbf{x}}) \equiv \langle \bar{\psi}\gamma^\mu\psi \rangle \tag{2.7}$$

and expand the interaction terms around their expectation values plus small fluctuations

$$\bar{\psi}\psi = \phi_S(\underset{\sim}{\mathbf{x}}) + \delta\phi_S \tag{2.8}$$

$$\bar{\psi}i\gamma_5\tau^a\psi = \phi_P^a(\underset{\sim}{\mathbf{x}}) + \delta\phi_P^a \tag{2.9}$$

$$\bar{\psi}\gamma^\mu\psi = n^\mu(\underset{\sim}{\mathbf{x}}) + \delta n^\mu. \tag{2.10}$$

Here $\underset{\sim}{\mathbf{x}}$ represents the four-position in Minkowski space. The fluctuations are assumed to be small, so only linear contributions of the δ-terms are considered. Then, squaring equation (2.8)–equation (2.10) reads

$$(\bar{\psi}\psi)^2 \approx -(\phi_S)^2(\underset{\sim}{\mathbf{x}}) + 2\phi_S(\underset{\sim}{\mathbf{x}})\bar{\psi}\psi \tag{2.11}$$

$$(\bar{\psi}i\gamma_5\tau^a\psi)^2 \approx -(\phi_P^a)^2(\underset{\sim}{\mathbf{x}}) + 2\phi_P^a(\underset{\sim}{\mathbf{x}})\bar{\psi}i\gamma_5\tau^a\psi \tag{2.12}$$

$$(\bar{\psi}\gamma^\mu\psi)^2 \approx -(n^\mu)^2(\underset{\sim}{\mathbf{x}}) + 2n^\mu(\underset{\sim}{\mathbf{x}})\bar{\psi}\gamma^\mu\psi. \tag{2.13}$$

The expectation values could, in principle, be both time and space-dependent, but here, only static condensates are considered. Hence, the condensates only depend on the three-position $\mathbf{x}$ in Euclidean space. The pseudo-scalar condensate will be considered only in 3-direction $\phi_P^a(\mathbf{x}) = \phi_P(\mathbf{x})\delta_{a,3}$, so a diagonal structure in flavor space is obtained. Furthermore, for the vector condensate in equation (2.13) only the time component is taken into account, that is $n^\mu(\mathbf{x}) = n(\mathbf{x})g^{\mu,0}$. In [23] it is shown that this is reasonable. The time component $n(\mathbf{x})$ can be identified with the density of the system and induces an effective shift in the chemical potential of the quarks. By applying the expressions above to equation (2.1), the mean-field Lagrangian is obtained:

$$\mathcal{L}_{\mathrm{MF}} + \mu\bar{\psi}\gamma_0\psi = \bar{\psi}S^{-1}\psi - \mathcal{V} \tag{2.14}$$

with the inverse quark-propagator in coordinate-space

$$S^{-1}(\mathbf{x}) = i\gamma^\mu\partial_\mu - m + \gamma_0\mu + 2g_s\left(\phi_S(\mathbf{x}) + i\gamma_5\tau^3\phi_P(\mathbf{x})\right) - 2\gamma_0 g_v n(\mathbf{x}) \tag{2.15}$$

and the contribution of the condensates

$$\mathcal{V}(\mathbf{x}) = g_s\left(\phi_S^2(\mathbf{x}) + \phi_P^2(\mathbf{x})\right) - g_v n^2(\mathbf{x}). \tag{2.16}$$

2.1. Thermodynamic potential

The preferred ground state of the system, for temperatures T and chemical potentials μ, can be extracted by minimizing the grand canonical potential per volume V of the model. It characterizes an open system, which allows the exchange of energy and particles with a heat bath for a specified temperature and chemical potential. The grand canonical potential[1] per volume is defined by

$$\Omega = -\frac{T}{V} \log \mathcal{Z}(T, \mu) \tag{2.17}$$

with the grand canonical partition function $\mathcal{Z}$. In mean-field approximation, it can be written in path-integral formalism [6]

$$\mathcal{Z}_{\mathrm{MF}} = \int \mathcal{D}\bar{\psi}\mathcal{D}\psi \exp\left(\int_0^{1/T} \mathrm{d}\tau \int_V \mathrm{d}^3x \left(\mathcal{L}_{\mathrm{MF}} + \mu\bar{\psi}\gamma_0\psi\right)\right) \tag{2.18}$$

with the imaginary time $\tau = it$ and the chemical potential μ. The resulting mean-field thermodynamic potential reads

$$\Omega_{\mathrm{MF}} = -\frac{T}{V} \log \int \mathcal{D}\bar{\psi}\mathcal{D}\psi \exp\left[\int_0^{1/T} \mathrm{d}\tau \int_V \mathrm{d}^3x \left(\bar{\psi}S^{-1}\psi - \mathcal{V}\right)\right]. \tag{2.19}$$

which is bilinear in the quark fields so the path integral can be performed and the resulting expression is given by

$$\Omega_{\mathrm{MF}} = -\frac{T}{V} \mathrm{Tr} \log\left(\frac{S^{-1}(\mathbf{x})}{T}\right) + \frac{1}{V} \int_V \mathrm{d}^3x \mathcal{V}(\mathbf{x}) \equiv \Omega_{\mathrm{kin}} + \Omega_{\mathrm{cond}} \tag{2.20}$$

where the two terms were identified as a kinetic and condensate contribution. The trace runs over color, flavor, Dirac and euclidean 4-volume space. The inverse propagator is diagonal in color space which will simply result in a factor $N_c = 3$. Before tracing over the other spaces, further steps are taken. Since the condensates are static, the temporal and spatial dependence of the inverse propagator can be isolated

$$S^{-1}(\mathbf{x}) = -i\partial_t - (H(\mathbf{x}) - \mu) \tag{2.21}$$

with the effective Hamiltonian

$$H(\mathbf{x}) - \mu = \gamma^0 \left[-i\boldsymbol{\gamma} \cdot \boldsymbol{\nabla} + m - 2g_s \left(\phi_S(\mathbf{x}) + i\gamma^5\tau_3\phi_P(\mathbf{x})\right)\right] - (\mu - 2g_v n(\mathbf{x})). \tag{2.22}$$

Since τ_3 is diagonal, the effective Hamiltonian can be written as a product in isospin space

$$H(\mathbf{x}) - \mu = \left(H^+(\mathbf{x}) - \mu\right) \otimes \left(H^-(\mathbf{x}) - \mu\right) \tag{2.23}$$

---

[1]For simplicity, it will be referred to as 'thermodynamic potential'.

with

$$H^{\pm}(\mathbf{x}) - \mu = \gamma^0 \left[-i\boldsymbol{\gamma} \cdot \boldsymbol{\nabla} + m - 2g_s \left(\phi_S(\mathbf{x}) \pm i\gamma^5 \phi_P(\mathbf{x}) \right) \right] - \tilde{\mu}(\mathbf{x}) = \begin{pmatrix} i\boldsymbol{\sigma} \cdot \boldsymbol{\nabla} - \tilde{\mu}(\mathbf{x}) & M^{\pm}(\mathbf{x}) \\ M^{\mp}(\mathbf{x}) & -i\boldsymbol{\sigma} \cdot \boldsymbol{\nabla} - \tilde{\mu}(\mathbf{x}) \end{pmatrix}.$$
(2.24)

In the last step, we used the Weyl representation of the γ-matrices. $\boldsymbol{\sigma}$ is the Pauli vector in spin space and $M^{\pm}(\mathbf{x})$ and $\tilde{\mu}(\mathbf{x})$ are the shifted mass and chemical potential, respectively, which are defined by

$$M^{\pm}(\mathbf{x}) = m - 2g_s \left(\phi_S(\mathbf{x}) \pm i\phi_P(\mathbf{x}) \right),$$
(2.25)

$$M^+(\mathbf{x}) \equiv M(\mathbf{x}) \quad \text{and} \quad M^-(\mathbf{x}) \equiv M^*(\mathbf{x}),$$
(2.26)

$$\tilde{\mu}(\mathbf{x}) = \mu - 2g_v n(\mathbf{x}).$$
(2.27)

H^+ and H^- are isospectral, so it is sufficient only to consider e.g. $H^+ \equiv H$ and multiply by a degeneracy factor $N_f = 2$.

In order to calculate the trace in Dirac and 4-volume space in equation (2.20) it is useful to switch to momentum space, where the quark fields, equation (2.25) and equation (2.27) can be expanded in Fourier series

$$\psi(x) = \frac{1}{\sqrt{V}} \sum_{p_n} \psi_{p_n} \, \mathrm{e}^{-ip_n x} = \frac{1}{\sqrt{V}} \sum_{\omega_n} \sum_{\mathbf{p}_n} \psi_{p_n} \, \mathrm{e}^{-i(\omega_n \tau - \mathbf{p}_n \mathbf{x})}$$
(2.28)

$$\bar{\psi}(x) = \frac{1}{\sqrt{V}} \sum_{p_n} \psi_{p_n} \, \mathrm{e}^{+ip_n x}$$
(2.29)

$$M^{\pm}(\mathbf{x}) = \sum_{\mathbf{q}_k} M^{\pm}_{\mathbf{q}_k} \, \mathrm{e}^{\pm i\mathbf{q}_k \mathbf{x}} \qquad \tilde{\mu}(\mathbf{x}) = \sum_{\mathbf{q}_k} \tilde{\mu}_{\mathbf{q}_k} \, \mathrm{e}^{\pm i2\mathbf{q}_k \mathbf{x}}.$$
(2.30)

Thereby, the condensates are assumed to be periodic in space. Here $\mathbf{q}_k$ are the discrete modulation momenta from the reciprocal lattice (R.L.). For the shifted potential, twice the wavenumber is expected, since the density from the solitonic solutions is known to oscillate with twice the frequency of the mass modulation. This is shown in figure 2.1. The factor 2 also occurred in the GL-analysis in the vicinity of the LP in [28].

The quark-fields satisfy the anti-periodic boundary condition $\psi(0, \mathbf{x}) = -\psi(\frac{1}{T}, \mathbf{x})$ which is imposed on the imaginary time direction. Hence, the Matsubara frequencies have the form $\omega_n = (2n+1)\pi T$. The effective Hamiltonian in momentum space becomes

$$H_{\mathbf{p}_m, \mathbf{p}_n} - \mu = \begin{pmatrix} -\boldsymbol{\sigma} \cdot \mathbf{p}_m \delta_{\mathbf{p}_m, \mathbf{p}_n} + \sum_{\mathbf{q}_k} \tilde{\mu}_{\mathbf{q}_k} \delta_{2\mathbf{q}_k, \mathbf{p}_m - \mathbf{p}_n} & \sum_{\mathbf{q}_k} M_{\mathbf{q}_k} \delta_{\mathbf{p}_m, \mathbf{p}_n + \mathbf{q}_k} \\ \sum_{\mathbf{q}_k} M^*_{\mathbf{q}_k} \delta_{\mathbf{p}_m, \mathbf{p}_n - \mathbf{q}_k} & \boldsymbol{\sigma} \cdot \mathbf{p}_m \delta_{\mathbf{p}_m, \mathbf{p}_n} + \sum_{\mathbf{q}_k} \tilde{\mu}_{\mathbf{q}_k} \delta_{2\mathbf{q}_k, \mathbf{p}_m - \mathbf{p}_n} \end{pmatrix}$$
(2.31)

with the in- and outgoing quark momenta $\mathbf{p}_n$ and $\mathbf{p}_m$, respectively.

Since quarks can exchange momenta by scattering off the condensate, the Hamiltonian is, in general, not diagonal in momentum space. This is reflected by the terms of equation (2.31) where the Kronecker-deltas contribute if the in- and outgoing momenta differ by $\mathbf{q}_k$ or $2\mathbf{q}_k$, respectively. Because the momentum space is infinite-dimensional, the diagonalization is highly non-trivial. But since H is hermitian, it can, in principle, be diagonalized. Therefore, further simplifications will be performed later. If the condensates are homogeneous ($M(\mathbf{x}) = const.$, $\tilde{\mu}(\mathbf{x}) = const.$) the quarks carry the same momenta and the Hamiltonian becomes diagonal in momentum space.
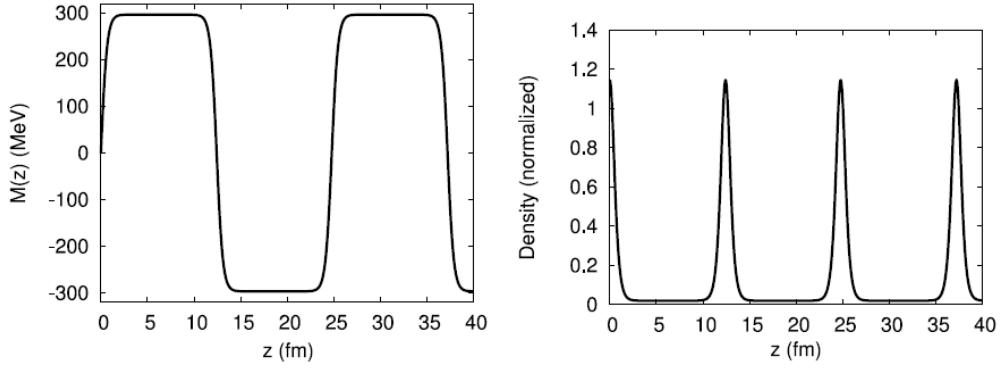
Figure 2.1.: Shape of the mass modulation (left) and corresponding quark number density (right) for the solitonic solutions at $\mu = 308\,\mathrm{MeV}$. The density has been normalized to the density in the restored phase at the given value of the chemical potential. The oscillation of the density is twice the mass modulation. Taken from [24]. Further details about the solitons are discussed in section 4.2.

By performing the trace in color and flavor space, the kinetic part of the thermodynamic potential becomes

$$\Omega_{\mathrm{kin}} = -\frac{T}{V} N_f N_c \sum_n \mathrm{Tr}_{\mathrm{Dirac},\mathbf{p}} \log\left(\frac{1}{T}\left(i\omega_n - (H - \mu)\right)\right) \tag{2.32}$$

$$= -\frac{T}{V} N_f N_c \sum_n \sum_{E_\lambda} \log\left(\frac{1}{T}\left(i\omega_n - E_\lambda\right)\right) \tag{2.33}$$

where E_λ are the eigenvalues of $H - \mu$ in Dirac and momentum space. S^{-1} is diagonal in frequency space, so the trace turned into a sum over ω_n. Performing the Matsubara sum yields

$$\Omega_{\mathrm{kin}} = -\frac{1}{V} N_f N_c \sum_{E_\lambda} \left[\frac{E_\lambda}{2} + T \log\left(1 + \exp\left(-\frac{E_\lambda}{T}\right)\right)\right]. \tag{2.34}$$

Using the definitions equation (2.25) and equation (2.27), the condensate part of the mean-field potential equation (2.20) leads to

$$\Omega_{\mathrm{cond}} = \frac{1}{V} \int_V \mathrm{d}^3\mathbf{x} \left(\frac{|M(\mathbf{x}) - m|^2}{4g_s} - \frac{|\tilde{\mu}(\mathbf{x}) - \mu|^2}{4g_v}\right) = \sum_{\mathbf{q}_k} \left(\frac{|M_{\mathbf{q}_k} - m\delta_{\mathbf{q}_k,0}|^2}{4g_s} - \frac{|\tilde{\mu}_{\mathbf{q}_k} - \mu\delta_{\mathbf{q}_k,0}|^2}{4g_v}\right). \tag{2.35}$$

2.2. Regularization

Due to the four-point interaction, the NJL model is not renormalizable. So to render diverging terms finite, it is necessary to apply a regularization scheme to the model. A detailed review of regularization schemes is stated in [30]. One possibility would be to use a 3-momentum cutoff. But this method is not suitable in inhomogeneous cases since the cutoff would restrict the maximal momentum and the maximum number of coupled momenta – it breaks Lorentz invariance. We therefore apply Pauli-Villars-regularization [31]. In this regularization-scheme E_λ is replaced by

$$E_\lambda \longrightarrow \sum_{j=0}^{3} c_j E_{\lambda,j} = \sum_{j=0}^{3} c_j \sqrt{E_\lambda^2 + j\Lambda^2} \tag{2.36}$$

with $c_0 = 1$, $c_1 = -3$, $c_2 = 3$, $c_3 = -1$ and a regulator Λ. The choice of parameters for deriving Λ and g_s, as well as their results, are shown in table 2.1. The coupling constant g_v will be treated as a variable.

$$
\begin{aligned}
M_{\text{vac}} &= 300\,\text{MeV} \\
f_\pi &= 88\,\text{MeV} \quad\longrightarrow\quad \begin{aligned} \Lambda &= 757.048\,\text{MeV} \\ g_s\Lambda^2 &= 6.002 \end{aligned} \\
T, \mu, m &= 0\,\text{MeV}
\end{aligned}
$$

Table 2.1.: The regulator Λ and coupling constant g_s are fixed for vanishing temperature T, chemical potential μ, and bare quark mass m. The vacuum quark mass M_{vac} and the pion decay constant f_π [33] are chosen as shown above.

The regularization scheme in equation (2.36) is standardly used in the case without vector interaction, where E_λ are defined as the eigenvalues of H. In our case, with included vector interaction, we defined E_λ as the eigenvalues of $H - \mu$ to include the vector condensate in the matrix. This leads to the problem that the Silver-blaze property [34] is not fulfilled. The Silver-blaze property states that M_0 should be independent of μ until particle excitation is possible, that is at $\mu \geq M_{\text{vac}} = 300\,\text{MeV}$ with the vacuum quark mass M_{vac}. The blue dotted lines in figure 2.2 show the results of the mass function and density in the homogeneous case in the chiral limit with $g_v/g_s = 0.5$ and $T = 0\,\text{MeV}$ with the regularization of equation (2.36). As we can see, M_0 starts to decrease long before $\mu = 300\,\text{MeV}$ and additionally, we get negative densities. To solve this issue we need to exclude the 0th component of $\tilde{\mu}$ from the matrix. Therefore, we use equation (2.27) to redefine the Hamiltonian matrix,

$$H - \mu = \tilde{H} - \tilde{\mu}_0, \tag{2.37}$$

and define $\tilde{E}_\lambda$ as the eigenvalues of $\tilde{H}$. Applying the Pauli-Villar-regularization to $\tilde{E}_\lambda$,

$$\tilde{E}_\lambda \longrightarrow \sum_{j=0}^{3} c_j \tilde{E}_{\lambda,j} = \sum_{j=0}^{3} c_j \sqrt{\tilde{E}_\lambda^2 + j\Lambda^2}, \tag{2.38}$$

yields correct results, as the red dotted lines in figure 2.2 show. In the case without vector interactions, the matrices $\tilde{H}$ and H coincide.
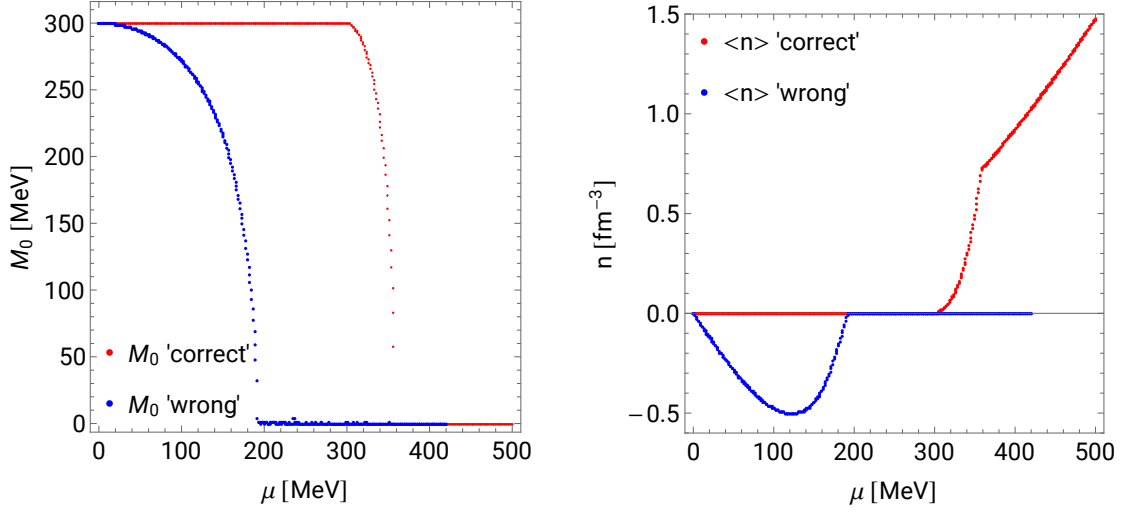
Figure 2.2.: Effective mass and density for the homogeneous case over μ, with the chemical potential still in the Pauli-Villars regularized terms (blue dotted) and the 'correct' solution (red dotted) for $g_v/g_s = 0.5$ and $T = 0\,\mathrm{MeV}$ in the chiral limit. The blue dotted line in the l.h.s. does not fulfill the Silver-blaze property. Furthermore, the wrong regularization yields a negative density.

Applying the redefinition of the Hamiltonian matrix and the regularization scheme to equation (2.34) yields

$$\Omega_{\mathrm{kin}} = -\frac{1}{V} N_f N_c \sum_{\tilde{E}_\lambda} \sum_{j=0}^{3} c_j \left\{ \frac{\tilde{E}_{\lambda,j} - \mathrm{sgn}(\tilde{E}_\lambda)\tilde{\mu}_0}{2} + T \log\left[1 + \exp\left(-\frac{\tilde{E}_{\lambda,j} - \mathrm{sgn}(\tilde{E}_\lambda)\tilde{\mu}_0}{T} \right) \right] \right\} \quad (2.39)$$

$$\underset{T \longrightarrow 0}{\rightsquigarrow} -\frac{1}{V} N_f N_c \sum_{\tilde{E}_\lambda} \sum_{j=0}^{3} c_j \left\{ \frac{\tilde{E}_{\lambda,j} - \mathrm{sgn}(\tilde{E}_\lambda)\tilde{\mu}_0}{2} + \left(\mathrm{sgn}(\tilde{E}_\lambda)\tilde{\mu}_0 - \tilde{E}_{\lambda,j} \right) \cdot \Theta\left[\mathrm{sgn}(\tilde{E}_\lambda)\tilde{\mu}_0 - \tilde{E}_{\lambda,j} \right] \right\}. \quad (2.40)$$

In equation (2.40) the limit for vanishing temperatures has been taken. In the case without vector interaction, it is common to split the thermodynamic potential into a divergent vacuum term and convergent medium term and sum only over the positive eigenvalues since the eigenvalue spectrum is symmetric around zero. In our case we have to regularize the complete kinetic part of the potential since in equation (2.34) the part with the logarithm which we would identify as the medium contribution is unbounded for negative eigenvalues. Since with vector interaction, the eigenvalue spectrum is shifted by the included $\tilde{\mu}_i$ in the Hamiltonian matrix, it is necessary to sum over all eigenvalues. In addition, the sgn-function between the round brackets in the 'medium part' in equation (2.40) can be omitted in the following steps: To obtain positive densities $\tilde{\mu}_0$ has to be positive and due to equation (2.38) $\tilde{E}_{\lambda,j}$ is always positive. As a result the Heaviside function only contributes for positive $\tilde{E}_\lambda$.

3. General preparations for numerical calculations

3.0.1. Lattice structure

As mentioned in section 2.1, the Hamiltonian is infinite-dimensional and thus cannot be diagonalized numerically without more ado. However, since the spatially modified condensates form a periodic structure in coordinate space, the Bloch theorem [35] can be used. The theorem says that the eigenstates, which belong to different vectors of the first Brillouin zone (B.Z.), are orthogonal. The periodic structure can be identified with a Bravais-lattice (B.L.) which forms a unit cell spanned by linear independent vectors $\mathbf{a}_i$, $i = 1, 2, 3$. The set of vectors $\mathbf{q}_k$ generate a reciprocal lattice (R.L.) which satisfy the condition $\frac{\mathbf{a}_i \cdot \mathbf{q}_k}{2\pi} \in \mathbb{Z}$. The B.Z. is the Wigner-Seitz (W.S.) primitive cell in the reciprocal lattice, which can be defined as the region of space that is closer to a single lattice point than to any other point. The in- and outgoing quark momenta can be written as

$$\mathbf{p}_n = \mathbf{k}_n + \mathbf{q}_n \tag{3.1}$$

$$\mathbf{p}_m = \mathbf{k}_m + \mathbf{q}_m \tag{3.2}$$

for $\mathbf{k}_n, \mathbf{k}_m \in$ B.Z. and $\mathbf{q}_n, \mathbf{q}_m \in$ R.L.. Considering the Hamiltonian equation (2.31) different momenta are coupled by $M_{\mathbf{q}_k}$ and $\tilde{\mu}_{\mathbf{q}_k}$ that differ by integer multiples of $\mathbf{q}_k$ of the R.L.. From the momentum difference

$$\mathbf{p}_m - \mathbf{p}_n = \underbrace{\mathbf{k}_m - \mathbf{k}_n}_{\in \text{B.Z.}} + \underbrace{\mathbf{q}_m - \mathbf{q}_n}_{\in \text{R.L.}} \tag{3.3}$$

it follows that this is the case if $\mathbf{k}_n = \mathbf{k}_m$ is satisfied. An example of the lattices and coupled in- and outgoing momenta in one-dimensions is shown in figure 3.1.
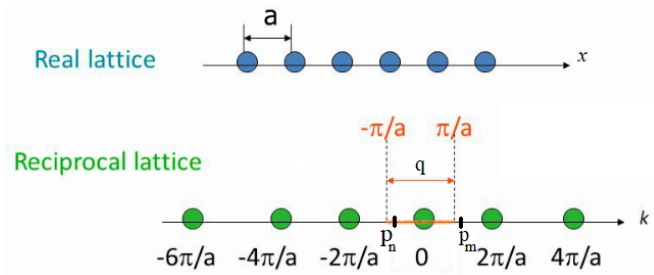

Figure 3.1.: One-dimensional lattice (blue) and generated reciprocal lattice (green) [36]. The R.L. elements are separated by q and the B.Z. is located in the red-marked area which is the Wigner-Seitz primitive cell. As an example, an ingoing momentum p_n, which is located in the B.Z., is coupled with an outgoing momentum p_m which differs by q.

As a consequence, the Hamiltonian can be decomposed into a sum of Hamiltonian blocks in the first Brillouin zone

$$\tilde{H} = \sum_{\mathbf{k}_n \in \text{B.Z.}} \tilde{H}(\mathbf{k}_n) \tag{3.4}$$

with each block characterized by a momentum of the B.Z.. So the momenta in the matrix $\tilde{H}(\mathbf{k}_n)$ can be mapped in a grid structure, where each element is separated from the others by a R.L. element. From this, the eigenvalues of $\tilde{H}$ are obtained by computing the eigenvalues of $\tilde{H}(\mathbf{k}_n)$ and summing over the B.Z.. Performing the infinite volume limit

$$\frac{1}{V} \sum_{\mathbf{k}_n \in \text{B.Z.}} \longrightarrow \int_{B.Z.} \frac{\mathrm{d}^3\mathbf{k}}{(2\pi)^3} \tag{3.5}$$

the thermodynamic potential can be written as

$$\Omega_{\text{kin}} = -N_f N_c \int_{\text{B.Z.}} \frac{\mathrm{d}^3\mathbf{k}}{(2\pi)^3} \sum_{\tilde{E}_\lambda} \sum_{j=0}^3 c_j \left\{ \frac{\tilde{E}_{\lambda,j}(\mathbf{k}) - \text{sgn}(\tilde{E}_\lambda)\tilde{\mu}_0}{2} + \left(\tilde{\mu}_0 - \tilde{E}_{\lambda,j}(\mathbf{k}) \right) \cdot \Theta \left[\text{sgn}(\tilde{E}_\lambda)\tilde{\mu}_0 - \tilde{E}_{\lambda,j}(\mathbf{k}) \right] \right\}. \tag{3.6}$$

3.0.2. Boosted eigenvalues and lower-dimensional modulations

If the condensate varies only in d dimensions the quark momenta $\mathbf{p}$ can be split into longitudinal $\mathbf{p}_\parallel$ and transversal $\mathbf{p}_\perp$ components with respect to the direction of quark condensate modulation

$$\mathbf{p} = \mathbf{p}_\parallel + \mathbf{p}_\perp. \tag{3.7}$$

In the case without vector interactions, one takes advantage of the Lorentz-symmetry of the system to simplify the matrix structure of H. This method was invented by Dominik Nickel [25]. In this case, the system is translationally invariant in the transversal directions. Thus, the corresponding operator $P_\perp$ commutes with H and exhibits simultaneous eigenstates $\Psi_{E_\lambda, \mathbf{p}_\perp}$, for which the $3+1$ dimensional eigenvalue problem

$$H\Psi_{E_\lambda, \mathbf{p}_\perp} = E_\lambda \Psi_{E_\lambda, \mathbf{p}_\perp} \tag{3.8}$$

$$P_\perp \Psi_{E_\lambda, \mathbf{p}_\perp} = \mathbf{p}_\perp \Psi_{E_\lambda, \mathbf{p}_\perp} \tag{3.9}$$

is satisfied. Now take $\Psi_{\lambda, \mathbf{0}}$ to be the eigenvector in the rest-frame of $\mathbf{p}_\perp$ with

$$H\Psi_{\lambda, \mathbf{0}} = \lambda \Psi_{\lambda, \mathbf{0}} \text{ and} \tag{3.10}$$

$$P_\perp \Psi_{\lambda, \mathbf{0}} = 0 \tag{3.11}$$

with the reduced eigenvalues λ. Take $\Lambda^\mu_{\ \nu}$ to be the Lorentz transformation that boosts the reduced eigenvector to the full $3+1$ eigenvector to receive the full-dimensional eigenvalues E_λ:

$$\Lambda^\mu_{\ \nu} \begin{pmatrix} \lambda \\ \mathbf{0} \end{pmatrix}^\nu = \begin{pmatrix} \lambda\sqrt{1 + \frac{\mathbf{p}_\perp^2}{\lambda^2}} \\ \mathbf{p}_\perp \end{pmatrix}^\mu = \begin{pmatrix} E_\lambda \\ \mathbf{p}_\perp \end{pmatrix}^\mu \tag{3.12}$$

$$\implies E_\lambda = \text{sgn}(\lambda)\sqrt{\lambda^2 + \mathbf{p}_\perp^2} \tag{3.13}$$

With included vector interactions Nickel's method is, in general, not applicable. This is discussed in detail in appendix A.2. A derivation of equation (3.13) based on the corresponding Hamiltonian can be found there, too.

So following expression for a d-dimensional modulation can be obtained:

$$\Omega_{\text{kin}}(\mu) = -N_f N_c \int \frac{\mathrm{d}^{3-d}\mathbf{p}_\perp}{(2\pi)^{3-d}} \int\limits_{\text{B.Z.}} \frac{\mathrm{d}^d\mathbf{k}}{(2\pi)^d} \sum_{\tilde{E}_\lambda} \sum_{j=0}^{3} c_j \left\{ \frac{\tilde{E}_{\lambda,j}(\mathbf{k},\mathbf{p}_\perp) - \text{sgn}(\tilde{E}_\lambda)\tilde{\mu}_0}{2} \right.$$
$$\left. + \left(\tilde{\mu}_0 - \tilde{E}_{\lambda,j}(\mathbf{k},\mathbf{p}_\perp) \right) \cdot \Theta \left[\text{sgn}(\tilde{E}_\lambda)\tilde{\mu}_0 - \tilde{E}_{\lambda,j}(\mathbf{k},\mathbf{p}_\perp) \right] \right\} \tag{3.14}$$

with

$$\tilde{E}_{\lambda,j}(\mathbf{k},\mathbf{p}_\perp) = \sqrt{\tilde{E}_\lambda^2(\mathbf{k},\mathbf{p}_\perp) + j\Lambda^2}. \tag{3.15}$$

In the case of constant vector condensates, that is for $\tilde{\mu}_n = 0$ with $n > 0$, the perpendicular momenta can be excluded from the Hamiltonian matrix, so the matrix structure and equation (3.14) can further be simplified drastically. This is discussed in appendix A.5. Thus, the computation time can be reduced significantly.

3.1. Deriving solutions in thermodynamic equilibrium

The solutions in thermodynamic equilibrium are given by the stationary points w.r.t. M_n and $\tilde{\mu}_n$ and the minimum w.r.t. q. One option to find these solutions is to derive gap equations, which are a coupled equation system, by the stationary conditions

$$\frac{\partial\Omega}{\partial M_n} = 0 \quad \text{and} \quad \frac{\partial\Omega}{\partial\tilde{\mu}_n} = 0 \tag{3.16}$$

and solve them via fix-point iteration. There, derivatives of the eigenvalues appear which are related to the eigenvectors of the system. Every Fourier coefficient leads to a gap-equation that depends on all other coefficients. So a rising number of included coefficients increases the size of the gap equation system and moreover the size of the matrix bandwidth, leading to numerically even more complicated eigenvector derivations. In total it impairs the computation time drastically. Since the numerical derivation of the eigenvalues is a lot faster than deriving the eigenvectors, in this thesis, we forgo the use of gap equations and derive the solutions by a minimizing algorithm instead. The potential will be minimized w.r.t. M_n and q and maximized w.r.t. $\tilde{\mu}_n$ – latter is equivalent to minimizing Ω w.r.t. $-\tilde{\mu}_n$. The maximization of $\tilde{\mu}_n$ is necessary since the potential only provides a maximum in $\tilde{\mu}_n$-direction, see figure 5.4. For the minimizations the *Nelder-Mead method* [37], also known as *downhill simplex method*, of *GSL* was used. The numerical diagonalization of the Hamiltonian matrix was performed with the *ZHBEV* routine of the *LAPACK* library [38].

4. One-dimensional modulations

4.1. General

The condensates will be considered to vary in one dimension. Without loss of generality, the modulation momentum is restricted to the third direction, $\mathbf{q} = nq\vec{e}_z$. So the ansätze of equation (2.30) become

$$M(z) = \sum_{n \in \mathbb{Z}} M_n \, \mathrm{e}^{inqz} \qquad \tilde{\mu}(z) = \sum_{n \in \mathbb{Z}} \tilde{\mu}_n \, \mathrm{e}^{2inqz} \,. \tag{4.1}$$

Then the effective Hamiltonian in momentum space reads

$$H_{p_m,p_n} = \begin{pmatrix} -(k+mq)\delta_{p_m,p_n} - \sum_{q_k} \tilde{\mu}_{q_k}\delta_{p_m,p_n+2q_k} & -p_\perp \delta_{p_m,p_n} \\ -p_\perp \delta_{p_m,p_n} & (k+mq)\delta_{p_m,p_n} - \sum_{q_k} \tilde{\mu}_{q_k}\delta_{p_m,p_n+2q_k} \\ \sum_{q_k} M_{q_k}^* \delta_{p_m,p_n-q} & 0 \\ 0 & \sum_{q_k} M_{q_k}^* \delta_{p_m,p_n-q} \end{pmatrix}$$

$$\begin{pmatrix} \sum_{q_k} M_{q_k}\delta_{p_m,p_n+q} & 0 \\ 0 & \sum_{q_k} M_{q_k}\delta_{p_m,p_n+q} \\ (k+mq)\delta_{p_m,p_n} - \sum_{q_k} \tilde{\mu}_{q_k}\delta_{p_m,p_n+2q} & -p_\perp \delta_{p_m,p_n} \\ -p_\perp \delta_{p_m,p_n} & -(k+mq)\delta_{p_m,p_n} - \sum_{q_k} \tilde{\mu}_{q_k}\delta_{p_m,p_n+2q_k} \end{pmatrix} \tag{4.2}$$

As discussed in section 3.0.1, the R.L. contains an infinite number of W.S. cells, so the modulated momenta have to be restricted to obtain a finite Hamiltonian matrix. Therefor, the modulated momenta get restricted to a numerical cutoff Λ_M

$$|Nq + k_z| \leq \Lambda_M \tag{4.3}$$

so the maximal size N of the Hamiltonian matrix is

$$N = \lfloor |\Lambda_M - k_z|/q \rfloor \tag{4.4}$$

where $\lfloor x \rfloor$ is the floor function, which means that for N the greatest integer smaller as or equal to x has to be taken. In the one-dimensional case, $d = 1$, equation (3.14) reads

$$\Omega_{\mathrm{kin}} = -\frac{N_f N_c}{(2\pi)^2} \int\limits_0^q \mathrm{d}k_z \int\limits_0^\infty \mathrm{d}p_\perp \, p_\perp \sum_{\tilde{E}_\lambda} \sum_{j=0}^3 c_j \left\{ \frac{\tilde{E}_{\lambda,j}(k_z,p_\perp) - \mathrm{sgn}(\tilde{E}_\lambda)\tilde{\mu}_0}{2} \right.$$
$$\left. + \left(\tilde{\mu}_0 - \tilde{E}_{\lambda,j}(k_z,p_\perp) \right) \cdot \Theta \left[\mathrm{sgn}(\tilde{E}_\lambda)\tilde{\mu}_0 - \tilde{E}_{\lambda,j}(k_z,p_\perp) \right] \right\}. \tag{4.5}$$

To simplify the numerical calculations, for high energies the eigenvalues are approximated by the homogeneous eigenvalues which is discussed in appendix A.3. Additionally, the asymptotic behavior of the integrand will be taken into advantage, see appendix A.4.

4.2. Ansätze and Hamiltonian matrix

We will consider the homogeneous case (HOM) and one-dimensional modulations for inhomogeneous condensates as follows: the chiral density wave (CDW), the cosine in average density approximation (ADA), the cosine with spatially modulated density and the solitonic solutions in ADA. The ansätze for the mass and chemical potential functions are shown in the table below:

	non-vanishing Fourier coefficients	$M(z)$	$\tilde{\mu}(z)$
HOM	$M_0, \tilde{\mu}_0$	M_0	$\tilde{\mu}_0$
CDW	$M_1, \tilde{\mu}_0$	$M_1\, e^{iqz}$	$\tilde{\mu}_0$
cosine, ADA	$M_{\pm 1}, \tilde{\mu}_0;\ M_{-1} = M_1,$	$2M_1\cos(qz)$	$\tilde{\mu}_0$
cosine, spat. mod. density	$M_{\pm 1}, \tilde{\mu}_0, \tilde{\mu}_{\pm 1};\ M_{-1} = M_1, \tilde{\mu}_{-1} = \tilde{\mu}_1$	$2M_1\cos(qz)$	$\tilde{\mu}_0 + \tilde{\mu}_1\cos(2qz)$

Table 4.1.: Non-vanishing Fourier coefficients and resulting functions of the mass and chemical potential ansätze for the homogeneous case, chiral density wave, cosine with 'average density approximation' and cosine with spatially modulated density (from top to bottom) in the chiral limit.

The factor 2 at the cosines comes from the definition of equation (2.30). The mass ansatz for the solitonic solutions in the chiral limit [39] is given by

$$M(z) = \Delta\nu\frac{\mathrm{sn}(\Delta z|\nu)\mathrm{cn}(\Delta z|\nu)}{\mathrm{dn}(\Delta z|\nu)}. \tag{4.6}$$

$\mathrm{sn}(\Delta z|\nu)$, $\mathrm{cn}(\Delta z|\nu)$ and $\mathrm{dn}(\Delta z|\nu)$ are the Jacobi elliptic functions, the parameter Δ relates to the mass amplitude and $\sqrt{\nu}$ is the elliptic modulus with $\nu \in [0,\ 1]$. Latter describes the shape of the modulation. The mass function of equation (4.6) and the corresponding density profile is shown in figure 2.1 exemplarily.

From equation (2.27) the space-dependent density $n(z)$ can be derived as

$$n(z) = \frac{\mu - \tilde{\mu}_0}{2g_v} - \frac{\tilde{\mu}_1}{2g_v}\cos(2qz) = \langle n\rangle - n_A\cos(2qz) \tag{4.7}$$

where the average density $\langle n\rangle$ and the density amplitude n_A can be identified.

For one-dimensional modulations with an arbitrary number of Fourier coefficients, the Hamiltonian matrix takes the form

$$H(k_z) = \begin{pmatrix} D_{-N}(M_0) & O(M_1, M_{-1}) & N(M_2, M_{-2}, \tilde{\mu}_1) & O(M_3, M_{-3}) & \cdots \\ O(M_{-1}, M_1) & D_{-N+1}(M_0) & \ddots & \ddots & \ddots \\ N(M_{-2}, M_2, \tilde{\mu}_1) & \ddots & \ddots & \ddots & N(M_2, M_{-2}, \tilde{\mu}_1) \\ O(M_{-3}, M_3) & \ddots & \ddots & D_{N-1}(M_0) & O(M_1, M_{-1}) \\ \vdots & \ddots & N(M_{-2}, M_2, \tilde{\mu}_1) & O(M_{-1}, M_1) & D_N(M_0) \end{pmatrix} \tag{4.8}$$

with the blocks

$$D_r(M_0) = \gamma_0\gamma_3(k_z + rq) + \gamma_0\gamma_1 p_\perp + \gamma_0 M_0 - \tilde{\mu}_0 \tag{4.9}$$

$$= \begin{pmatrix} -(k_z + rq) - \tilde{\mu}_0 & -p_\perp & M_0 & 0 \\ -p_\perp & (k_z + rq) - \tilde{\mu}_0 & 0 & M_0 \\ M_0 & 0 & (k_z + rq) - \tilde{\mu}_0 & -p_\perp \\ 0 & M_0 & -p_\perp & -(k_z + rq) - \tilde{\mu}_0 \end{pmatrix}, r \in \mathbb{Z} \tag{4.10}$$

$$O(M_{\pm n}, M_{\mp n}) = \gamma_0\frac{1}{2}\left[M_{\pm n} + M_{\mp n} + \gamma_5 M_{\mp n} - \gamma_5 M_{\pm n}\right] \tag{4.11}$$

$$= \begin{pmatrix} 0 & 0 & M_{\mp n} & 0 \\ 0 & 0 & 0 & M_{\mp n} \\ M_{\pm n} & 0 & 0 & 0 \\ 0 & M_{\pm n} & 0 & 0 \end{pmatrix}, n \text{ odd} \tag{4.12}$$

$$N(M_{\pm n}, M_{\mp n}, \tilde{\mu}_{n/2}) = \gamma_0\frac{1}{2}\left[M_{\pm n} + M_{\mp n} + \gamma_5 M_{\mp n} - \gamma_5 M_{\pm n}\right] - \tilde{\mu}_{n/2} \tag{4.13}$$

$$= \begin{pmatrix} -\tilde{\mu}_{n/2} & 0 & M_{\mp n} & 0 \\ 0 & -\tilde{\mu}_{n/2} & 0 & M_{\mp n} \\ M_{\pm n} & 0 & -\tilde{\mu}_{n/2} & 0 \\ 0 & M_{\pm n} & 0 & -\tilde{\mu}_{n/2} \end{pmatrix}, n \text{ even.} \tag{4.14}$$

5. Chiral limit

Here, we will briefly discuss the findings of [22–24] with regard of the homogeneous solution, the CDW and the cosine with spatially modulated density based on the free energies at $g_v/g_s = 0.0$, $g_v/g_s = 0.3$ and $g_v/g_s = 0.5$ in the chiral limit. Thereafter, we study these findings in terms of the thermodynamic potential at $g_v/g_s = 0.0$ and $g_v/g_s = 0.3$.

5.1. Free energies

In figure 5.1, the free energies for the homogeneous case (blue dashed-dotted), the CDW (black dashed), the cosine (red dashed) and the solitonic solutions (green dot-dashed) are shown for $g_v/g_s = 0.0$ in the upper panel. In the lower panels the free energies for the same ansätze are shown for $g_v/g_s = 0.3$ and $g_v/g_s = 0.5$, except of the solitonic solutions. The CDW has a homogeneous density, so for $g_v/g_s \neq 0.0$ we consider the ADA which is an exact approximation for the CDW. This is not the case for the cosine, so for $g_v/g_s \neq 0.0$ we consider the cosine with spatially modulated density. The free energy plots exhibit a homogeneous phase where the homogeneous solution is the most favored. On the left phase boundary the CDW, cosine perform a first order transition (not shown in the plots) into the inhomogeneous phase. The solitons arise by a second order transition. A first order transition is characterized by a crossing of the free energies of two solutions between which the system swaps. At a second order transition the free energy of the next favored solution merges from the previously favored one. With rising μ the free energies of the solutions merge into the chirally restored phase by a second order transition where all solutions coincide. For $g_v/g_s = 0.0$ the solitonic and sinusoidal solutions almost degenerate so the cosine is a good approximation.

The more favored solution is manifested by a lower free energy. At $g_v/g_s = 0.0$ the CDW is disfavored against the real modulations in the whole inhomogeneous window. Turning on the vector interaction strength to $g_v/g_s = 0.3$ yields a region in the beginning of the inhomogeneous phase where the CDW is favored against the cosine, up to a specific chemical potential where the cosine is favored against the CDW. At even higher vector couplings, e.g. $g_v/g_s = 0.5$, the CDW is favored against the cosine in the whole inhomogeneous window. For $g_v/g_s = 0.0$ the solitonic solution is a self-consistent solution and the most favored solution so far, for $g_v/g_s \neq 0.0$ the solitonic solution is not self-consistent.

Due to the small modulation momentum q and consequently very large matrix size in the beginning of the inhomogeneous phase, it was not possible to perform calculations there for the CDW and cosine. Thus, the plots show gaps in the vicinity of the first order transition. For the corresponding diagrams where q and the Fourier coefficients of the mass function and the density are plotted against μ we refer to the stated literature.
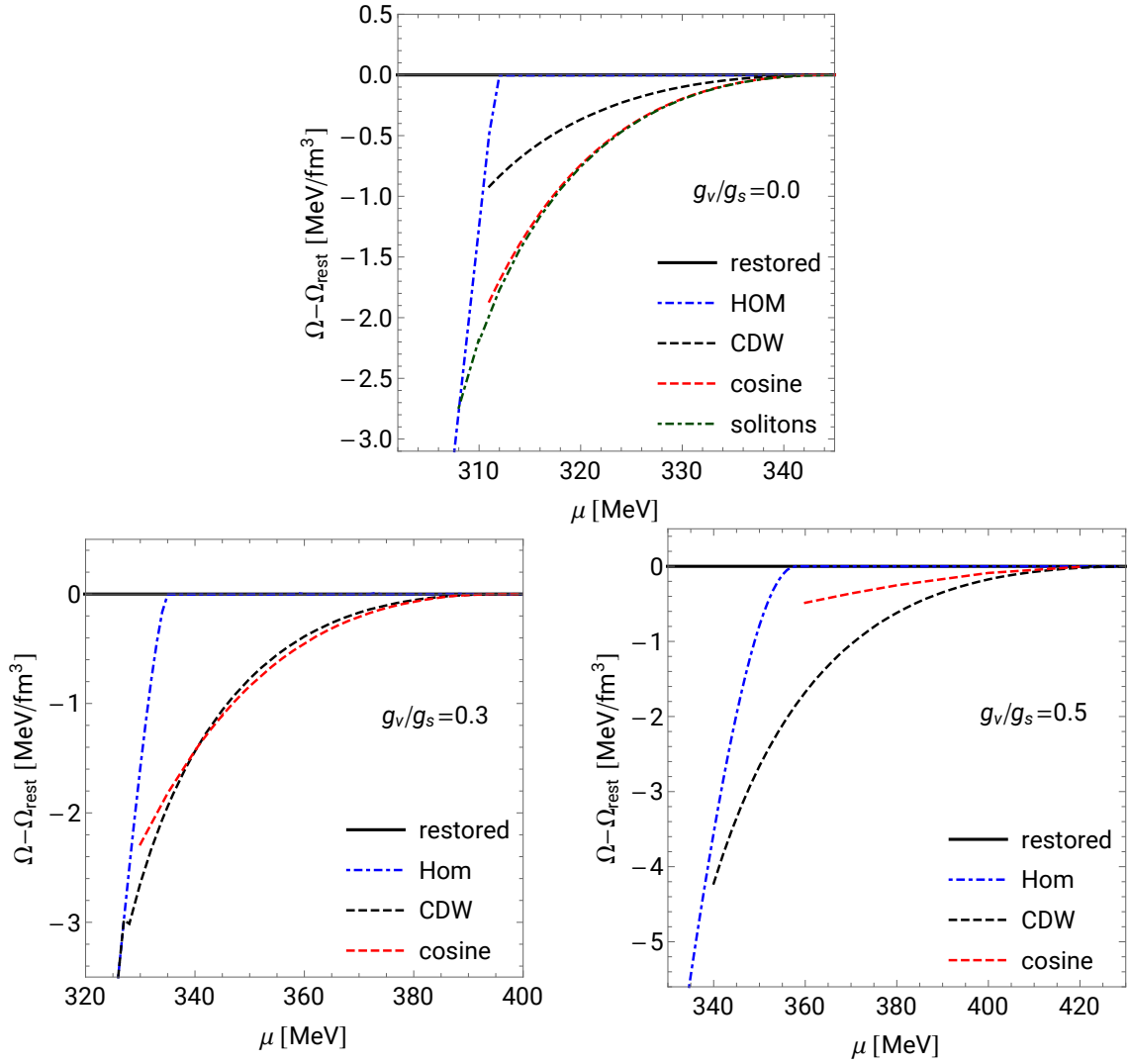
Figure 5.1.: Free energies for the homogeneous case, the CDW and the cosine at $g_v/g_s = 0.0$ (top), $g_v/g_s = 0.3$ (bottom left) and $g_v/g_s = 0.5$ (bottom right). Additionally, the free energy of the solitons are shown at $g_v/g_s = 0.0$. For $g_v/g_s \neq 0.0$ the CDW was considered in ADA and the cosine with spatially modulated density.

5.2. Homogeneous case

To get a deeper understanding of the discussed findings, we can plot the thermodynamic potential in the space of the relevant coefficients. This has been done for the homogeneous case quite extensively, for example in [30, 32], so we will restrict the discussions to the inhomogeneous case.

5.3. CDW and cosine

5.3.1. Vanishing vector interactions

For the investigations of the CDW and the cosine, at first for $g_v/g_s = 0.0$, we plot the thermodynamic potential in the space of the coefficients M_1 and M_{-1}. This is shown in the left picture of figure 5.2 where for each value of M_1 and M_{-1} the thermodynamic potential was minimized with respect to q. In the chiral limit, the CDW is a self-consistent solution, but as we can see it is not a stable solution but only a saddle point, that is at $(M_1, M_{-1}) \approx (72, 0)\text{MeV}$. The global minimum in the M_1-M_{-1}-plane at $(M_1, M_{-1}) \approx (74, 74)\text{MeV}$ is occupied by the cosine since in this point it is $M_1 = M_{-1}$. Since the global minimum is energetically more favored than the saddle point the cosine is more favored. The M_0 coefficient is trivially zero in both cases. In the right picture of figure 5.2 the thermodynamic potential was minimized w.r.t. q and M_1 for each value of M_{-1}. Here, the CDW occupies the maximum at $M_{-1} = 0\,\text{MeV}$ and the cosine the minimum at $M_{-1} \approx 74\,\text{MeV}$ which reflects the results from the left picture consistently.
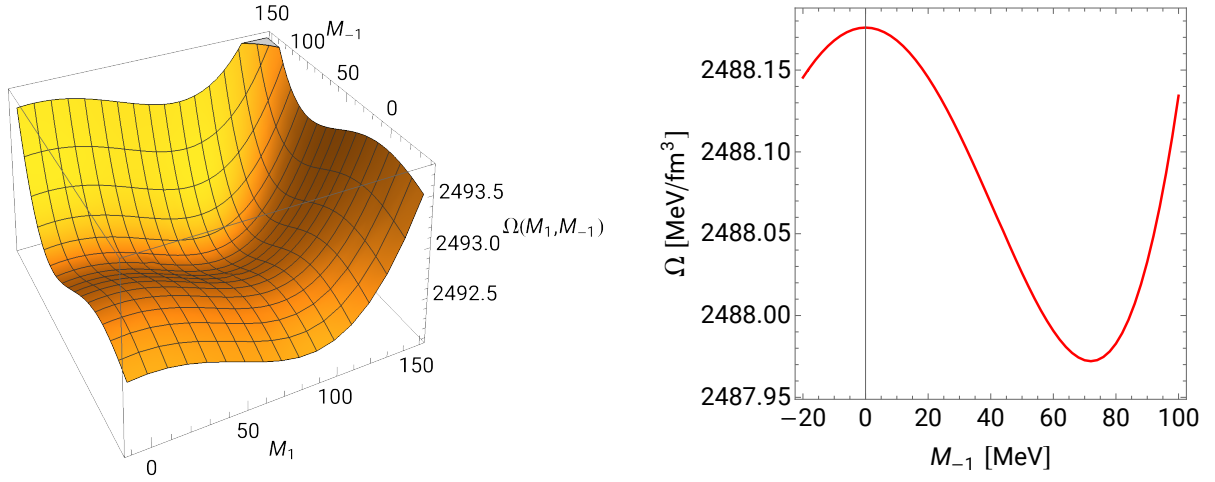

Figure 5.2.: Left: Thermodynamic potential plotted in the M_1-M_{-1}-plane, minimized with respect to q. Right: Thermodynamic potential plotted in M_{-1}-direction, minimized with respect to q and M_1. Both are in the chiral limit at $\mu = 325\,\text{MeV}$ and for $g_v/g_s = 0.0$.

5.3.2. Non-vanishing vector interactions

In figure 5.3 the thermodynamic potential is shown for $g_v/g_s = 0.3$ in the beginning, middle and more to the end of the inhomogeneous phase: at $\mu = 335\,\text{MeV}$ (top left), $\mu = 341\,\text{MeV}$ (top right) and $\mu = 360\,\text{MeV}$ (bottom) respectively. For each value of M_{-1} the thermodynamic potential was minimized w.r.t. both q and M_1 and maximized w.r.t. both $\tilde{\mu}_0$ and $\tilde{\mu}_1$. At $\mu = 335\,\text{MeV}$ both the CDW and the cosine with spatially dependent density occupy minima, at $(M_1, M_{-1}) \approx (145, 0)\text{MeV}$ and $(M_1, M_{-1}) \approx (95, 95)\text{MeV}$ respectively. Since the CDW is favored here, its minimum lies below the one of the cosine. It is quite special that the potential exhibit two minima in the inhomogeneous phase, but the former investigations showed that both the cosine and the favored solution occupy minima w.r.t. the corresponding Fourier coefficients, so it is not an unexpected result. Shortly after the first order transition to the region where the cosine is

favored, at $\mu = 341\,\mathrm{MeV}$, both solutions again occupy a minimum but now the minimum of the cosine lies slightly below since it is more favored. At higher chemical potentials, e.g. $\mu = 360\,\mathrm{MeV}$, the kind of extremum of the CDW changes into a maximum. The picture at $\mu = 335\,\mathrm{MeV}$ indicates a third minimum of the thermodynamic potential at larger M_{-1}. There, we would find a minimum of the CDW with $M_1 = 0$ and $M_{-1} \neq 0$. We should also find those extrema in the other two plots, but due to the computationally challenging calculations, we had to restrict the range in M_{-1}-direction as shown.

The fact that both CDW and cosine with spatially modulated density occupy minima in the beginning and middle of the inhomogeneous phase has an important impact on finding the energetically favored solution. As minima both are stable solutions, so starting the minimizing routine with 'wrong' initial values will likely lead to a solution that is not energetically favored. Especially, this becomes critical in the region where the free energies lie close to each other, e.g. at $\mu \approx 341\,\mathrm{MeV}$. So it is not ensured to find the cosine if the initial values are close to the CDW and vice versa. Consequently, it is not recommended to trust the result of the minimization solely but it highly reasons the analysis of the thermodynamic potential.
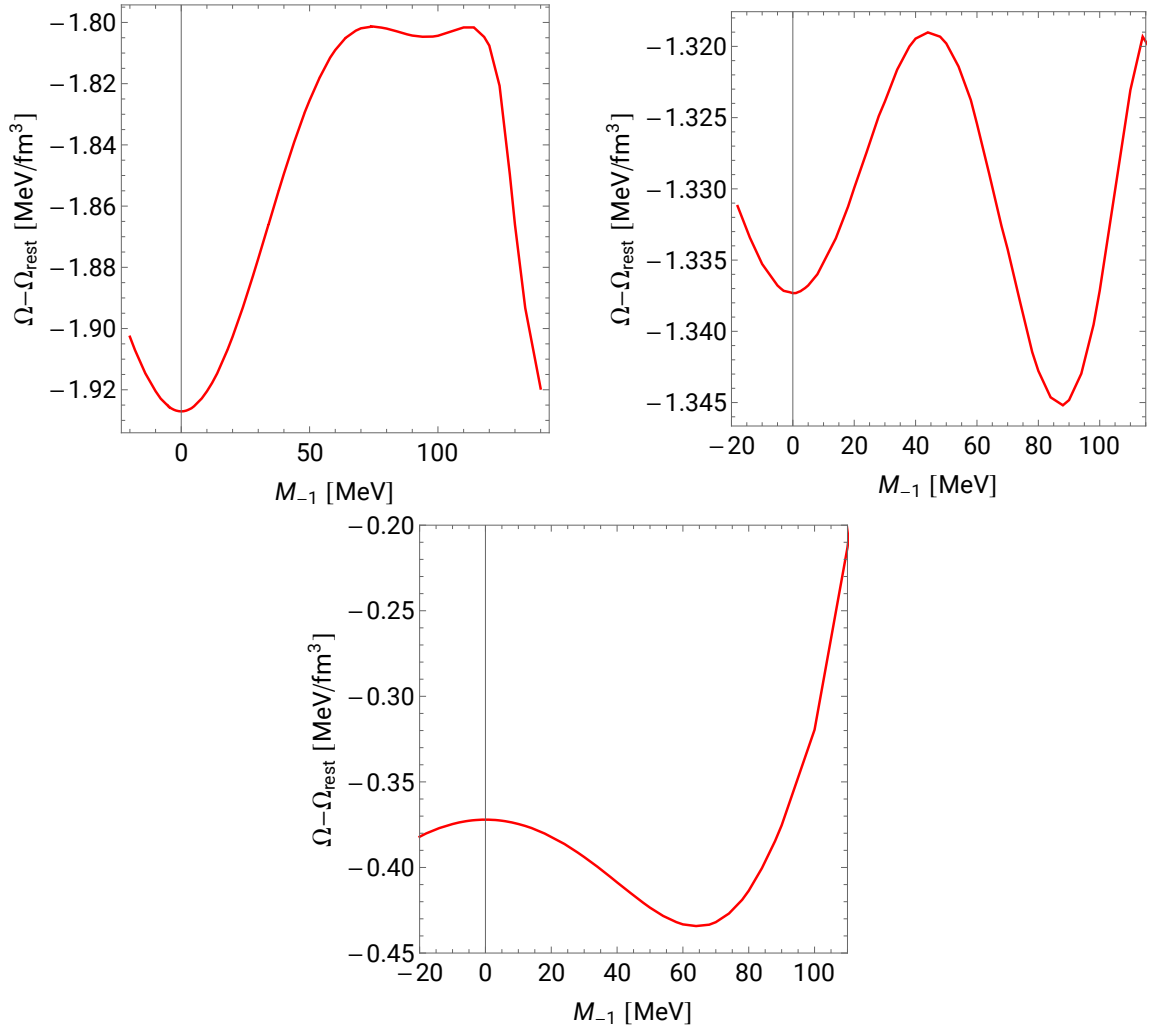

Figure 5.3.: Thermodynamic potential in the chiral limit in M_{-1}-direction at $\mu = 335\,\mathrm{MeV}$ (top left), $\mu = 341\,\mathrm{MeV}$ (top right) and $\mu = 360\,\mathrm{MeV}$ (bottom) for $g_v/g_s = 0.3$, minimized with respect to q and M_1 and maximized with respect to $\tilde{\mu}_0$ and $\tilde{\mu}_1$.

Density

For the calculations with non-vanishing vector condensates, we had to apply an ansatz for the density to the CDW and cosine. The CDW is known to have a homogeneous density so the ADA was applied. The homogeneity of the density becomes evident by finding a vanishing density amplitude n_A, see figure 5.4 left. In contrast, the density of the cosine is space-depending. This is reflected by finding the maxima with respect to both $\langle n \rangle$ and n_A at non-zero values, figure 5.4 right. There, we observe that the thermodynamic potential only provides maxima w.r.t. $\tilde{\mu}_n$ which was already discussed in section 3.1.
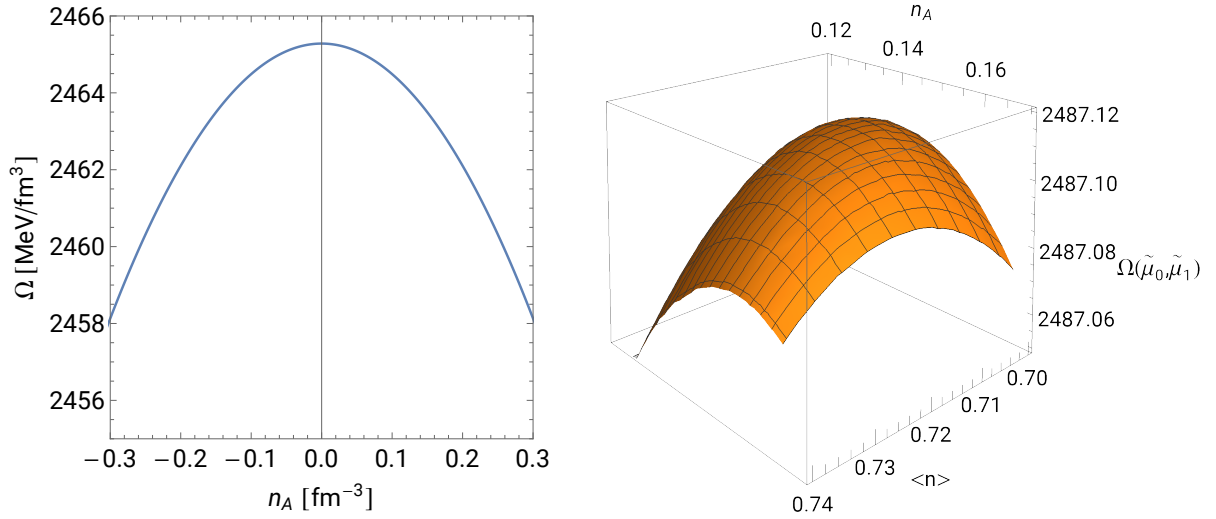

Figure 5.4.: Thermodynamic potential in n_A-direction for the CDW (left) and in the $\langle n \rangle$-n_A-plane for the cosine. Both are in the chiral limit at $\mu = 345\,\mathrm{MeV}$ for $g_v/g_s = 0.3$. For each point in the r.h.s. plane the thermodynamic potential was minimized with respect to q and M_1 and for each point in the l.h.s. plot it was additionally maximized with respect to $\tilde{\mu}_0$.

6. Explicitly broken chiral symmetry

In this section we introduce a non-vanishing bare quark mass of $m = 5\,\mathrm{MeV}$. The consequences regarding the homogeneous case, CDW and cosine ansatz without vector interaction, that is for $g_v/g_s = 0.0$, was already discussed in [22]. Here, we will investigate the thermodynamic potential for $g_v/g_s = 0.3$, compare it with the case of $g_v/g_s = 0.0$ and discuss the implications that emerge from the results. Additionally, we compare the μ-q,M-diagrams as well as the densities for the CDW and cosine for $g_v/g_s = 0.0$ and $g_v/g_s = 0.3$. Due to the numerical challenges that occur if we include $\tilde{\mu}_1$ we will restrict the calculations to the ADA.
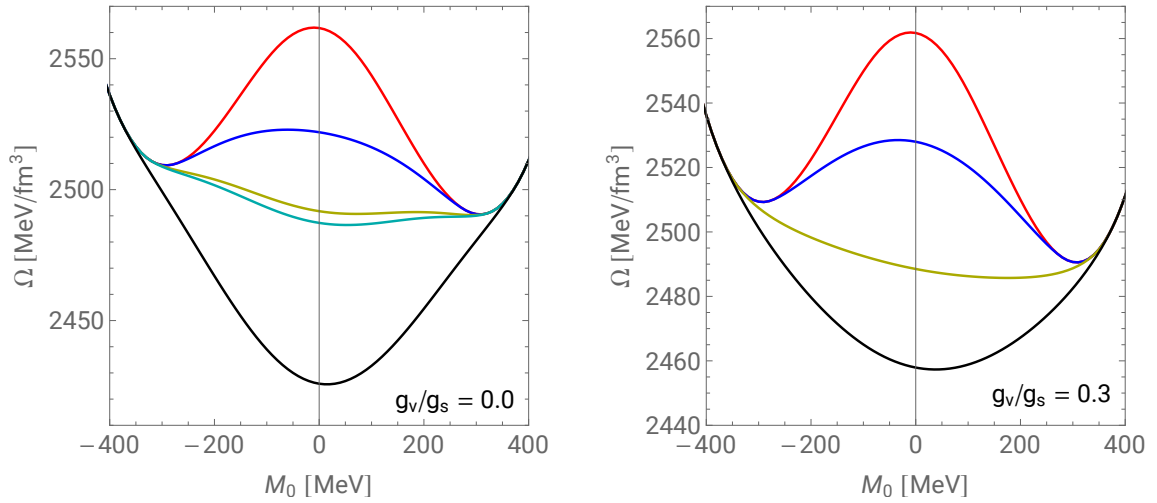
6.1. Homogeneous case

Figure 6.1.: Thermodynamic potential for several μ plotted against M_0. Chemical potentials on the left: $100\,\mathrm{MeV}$ (red), $280\,\mathrm{MeV}$ (blue), $322\,\mathrm{MeV}$ (dark yellow), $327\,\mathrm{MeV}$ (cyan), $380\,\mathrm{MeV}$ (black). Chemical potentials on the right: $100\,\mathrm{MeV}$ (red), $280\,\mathrm{MeV}$ (blue), $345\,\mathrm{MeV}$ (dark yellow), $380\,\mathrm{MeV}$ (black).

The thermodynamic potentials for $g_v/g_s = 0.0$ and $g_v/g_s = 0.3$ for several μ are shown in figure 6.1. In both pictures we see the broken symmetry of the thermodynamic potential due the non-vanishing m, with the consequence that the negative solutions for M_0 are always disfavored. Initially (red, blue) the global minimum is located at $M_0 \approx 307\,\mathrm{MeV}$ and the maximum is slightly shifted from $0\,\mathrm{MeV}$. The left picture suggests a first order transition, this is familiar with the chiral limit for small and vanishing vector interactions. In the region of $\mu = 322\,\mathrm{MeV}$ (dark yellow) and $\mu = 327\,\mathrm{MeV}$ (cyan) the thermodynamic

potential exhibit two minima for $M_0 > 0$, at $M_0 \approx 20\,\mathrm{MeV}$ and $M_0 \approx 300\,\mathrm{MeV}$, from which the latter (first) one is energetically favored at $\mu = 322\,\mathrm{MeV}$ ($\mu = 327\,\mathrm{MeV}$). In the right picture the initial minimum smoothly shifts to smaller values which corresponds to a crossover.

In figure 6.2 the μ-M_0-diagrams and self-consistent densities for the homogeneous case are shown for $g_v/g_s = \{0.0,\ 0.1,\ 0.3\}$. As we have seen before, the M_0 coefficient starts at $\approx 307\,\mathrm{MeV}$ while the density vanishes at this point. From a slightly larger value than $\mu = M_\mathrm{vac}$ they start to fall/rise smoothly. In our case[1], due to the Silver-Blaze-property, the parameters cannot change at $\mu < M_\mathrm{vac}$. For $g_v/g_s = \{0.0,\ 0.1\}$ we find M_0 and n to be discontinuous at $\mu \approx 320\,\mathrm{MeV}$ and $\mu \approx 330\,\mathrm{MeV}$, respectively. At larger g_v/g_s we do not find a discontinuous behavior anymore but a crossover where the quantities are continuous. So the vector interaction weakens the first order transition until it becomes a crossover. This behavior is familiar from the chiral limit case, with the exception that we would find a second order transition there. In contrast to the chiral limit, there is no chirally restored phase since a non-vanishing m breaks the chiral symmetry explicitly. This is reflected in M_0 not converging to 0 after the first order transition or the crossover with rising μ. It just converges to small values but never reaches 0. This indicates that the chiral symmetry is only approximately fulfilled. As we can see, rising the vector interaction strength retards the transitions to higher μ and suppresses the density after the phase transitions. This is intuitively clear since it is a repulsive interaction, so the quarks are forced to be uniformly distributed farther away from each other.
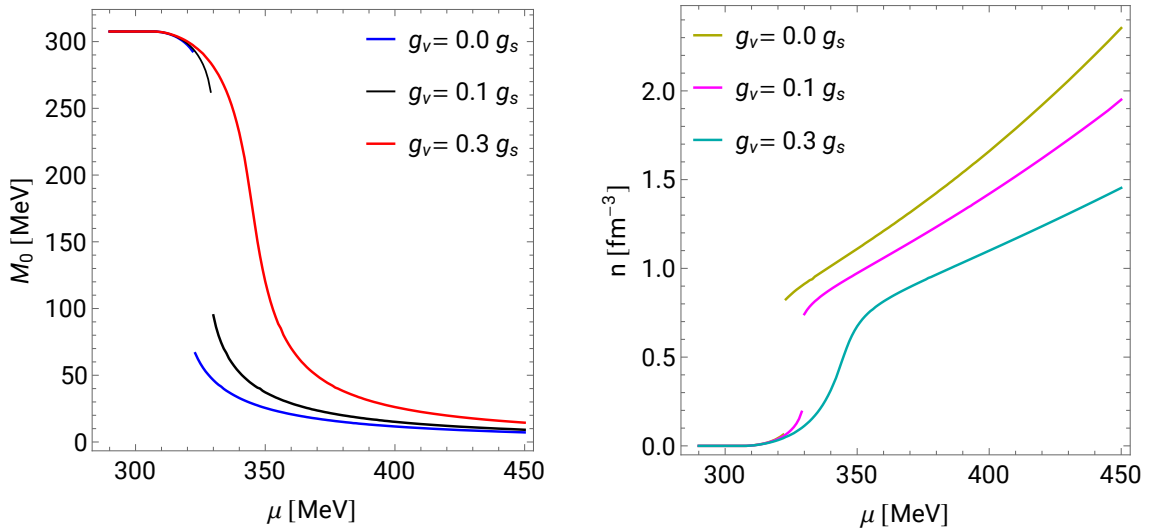

Figure 6.2.: Effective masses (left) and self-consistent densities (right) plotted against μ with $m = 5\,\mathrm{MeV}$.

6.2. CDW

As we already discussed, the CDW is a self-consistent solution in the chiral limit and has a homogeneous density, so the ADA is an exact approximation. Things change as soon as a non-vanishing m or non-vanishing vector interactions are introduced as we will discuss in the following. In figure 6.3 (left) the M_{-1}-M_0-plane of the thermodynamic potential is shown for $g_v/g_s = 0.3$ at $\mu = 360\,\mathrm{MeV}$ in ADA, that is for $\tilde{\mu}_1 = 0$.

---

[1]The parameters could change at smaller chemical potentials if there was a phase transition to a solution with a smaller mass than our M_vac.

For each point in the plane we minimized w.r.t. both M_1 and q and maximized w.r.t. $\tilde{\mu}_0$. The CDW has a maximum w.r.t. M_{-1} at $(M_{-1},\ M_0) \approx (0,\ 0)$MeV but this does not correspond to a minimum, nor a maximum, w.r.t. M_0, so it is not an extremal point in this plane. Then, it would be intuitive to extend the CDW by a constant shift M_0 and move in its minimum: $(M_{-1},\ M_0) \approx (0,\ 66)$MeV. But here we find that the CDW has no maximum in M_{-1} anymore. This becomes evident by the r.h.s. of figure 6.3, where the thermodynamic potential is plotted in M_{-1}-direction – there, for each point the potential was additionally minimized w.r.t. M_0. So neither the 'standard' CDW nor the 'extended' CDW is a self-consistent solution. In the minimum of both plots in figure 6.3 the Fourier coefficients of the mass function have the values $(M_{-1},\ M_0,\ M_1) \approx (66,\ 77,\ 66)$MeV, this corresponds to a cosine with a constant shift.
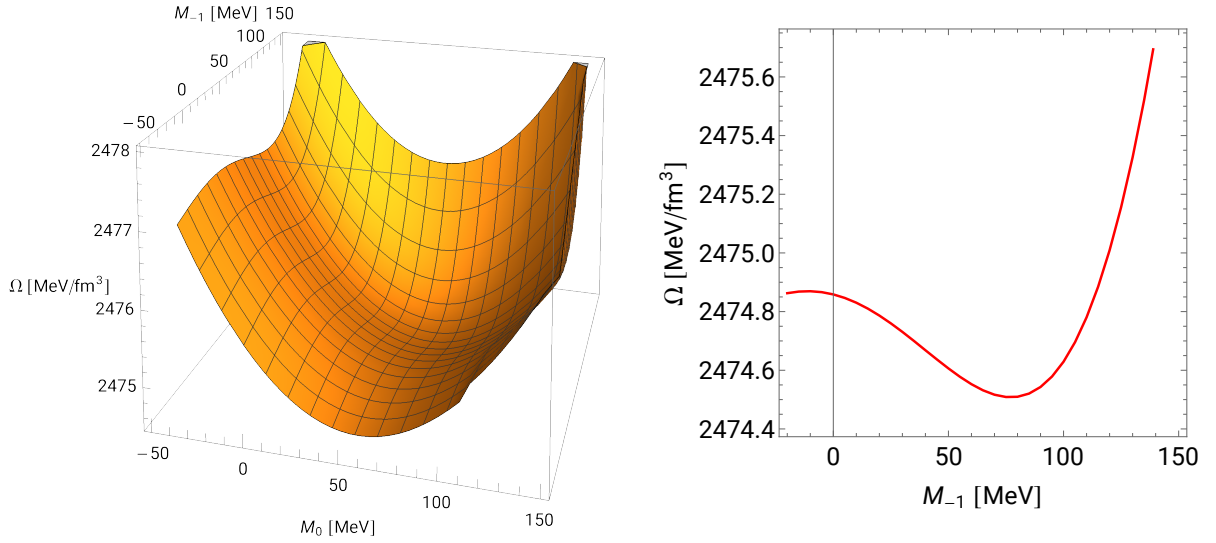

Figure 6.3.: M_{-1}-M_0-plane (left) and M_{-1}-direction (right) of the thermodynamic potential at $\mu = 360\,\mathrm{MeV}$ for $g_v/g_s = 0.3$ and with $m = 5\,\mathrm{MeV}$. For each point in the l.h.s. plane the thermodynamic potential was minimized w.r.t. both M_1 and q and maximized w.r.t. $\tilde{\mu}_0$. For each point in the r.h.s. plot it was additionally minimized w.r.t. M_0.

Furthermore, by comparing the free energies of the standard CDW and homogeneous solution for $g_v/g_s = 0.0$ and $g_v/g_s = 0.3$ for several m, see figure 6.4, it follows that there is a critical bare mass above which the CDW is disfavored against the homogeneous solution. This appears at $m \gtrsim 3\,\mathrm{MeV}$ and is just little affected by the vector interactions. So in our case of $m = 5\,\mathrm{MeV}$ it is not useful to consider the CDW any longer. Instead, we will extend the CDW by the constant shift M_0 and label it 'CDW+'. Also, the cosine will be extended by M_0 which we will label with 'cosine+'.

6.2.1. Extended CDW

In figure 6.5 the modulation momentum q, the Fourier coefficients M_0 and M_1 (top) and the average density (bottom) of the CDW+ ansatz against μ are shown for $g_v/g_s = 0.0$ (left) and $g_v/g_s = 0.3$ (right). We can identify the homogeneous broken phases where M_1 is zero and an inhomogeneous phase where M_1 differs from 0. At the left phase boundary the phase transition occurs by a first order transition. This kind of phase transition is characterized by a discontinuity of the Fourier coefficients. Without vector interaction, the coefficients decline with a rising modulation momentum and M_1 takes slightly larger values than M_0,
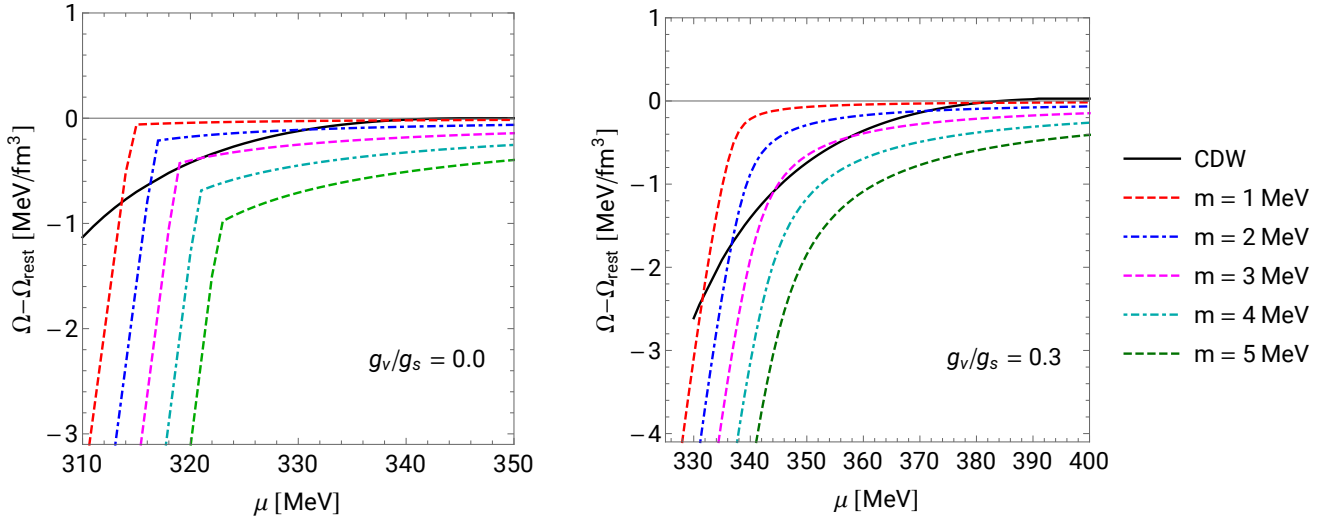
Figure 6.4.: Free energies for the homogeneous solution (colored) and the standard CDW (black) for $g_v/g_s = 0.0$ (left) and $g_v/g_s = 0.3$ (right) for $m = \{1, 2, 3, 4, 5\}$ MeV. The CDW is just listed once since its free energy is not affected by m.

the modulation momentum q is located in the range of 400–500 MeV. At a specific chemical potential the inhomogeneous phase becomes disfavored against the homogeneous phase, M_1 drops to zero by a second order transition while M_0 remains non-zero. In the chiral limit, we would find a chirally restored phase here, but due to the non-vanishing m an exact order parameter does not exist for the distinction between the homogeneous broken and the chirally restored phase where the condensates would vanish.

For $g_v/g_s = 0.3$ right after the phase transition at the left phase boundary M_0 is twice as large as M_1 and q starts with ~ 130 MeV. Consequently, the vector interaction drastically reduces the oscillations of the mass function. The density is strongly suppressed in the beginning of the inhomogeneous phase by the vector interaction. This is analogous to the investigations of the homogeneous case, where the vector interactions suppressed the quark number density right after the transitions. With rising chemical potential M_0 begins to decline while M_1 slightly rises until both coefficients cross each other and decline together just as we observed for $g_v/g_s = 0.0$. In the beginning of the inhomogeneous phase, between $\mu = 341$ MeV and 343 MeV, q exhibits a very large slope. But afterward, its slope is massively reduced and q again rises up to 500 MeV. Just as it was found in the chiral limit the vector interaction enlarges the inhomogeneous phase. The r.h.s. of figure 6.5 exhibit a gap at $\mu = 340$ MeV since q becomes so small that the derivations at this chemical potential were not possible. It is reasonable to ask if the vector interactions can weaken the first order transition to the inhomogeneous phase so it almost becomes a second order transition. Unfortunately, this would require calculations in the region of $q = 0$ which would lead to a diverging size of the Hamiltonian matrix so at the moment it is not possible to examine this suggestion.
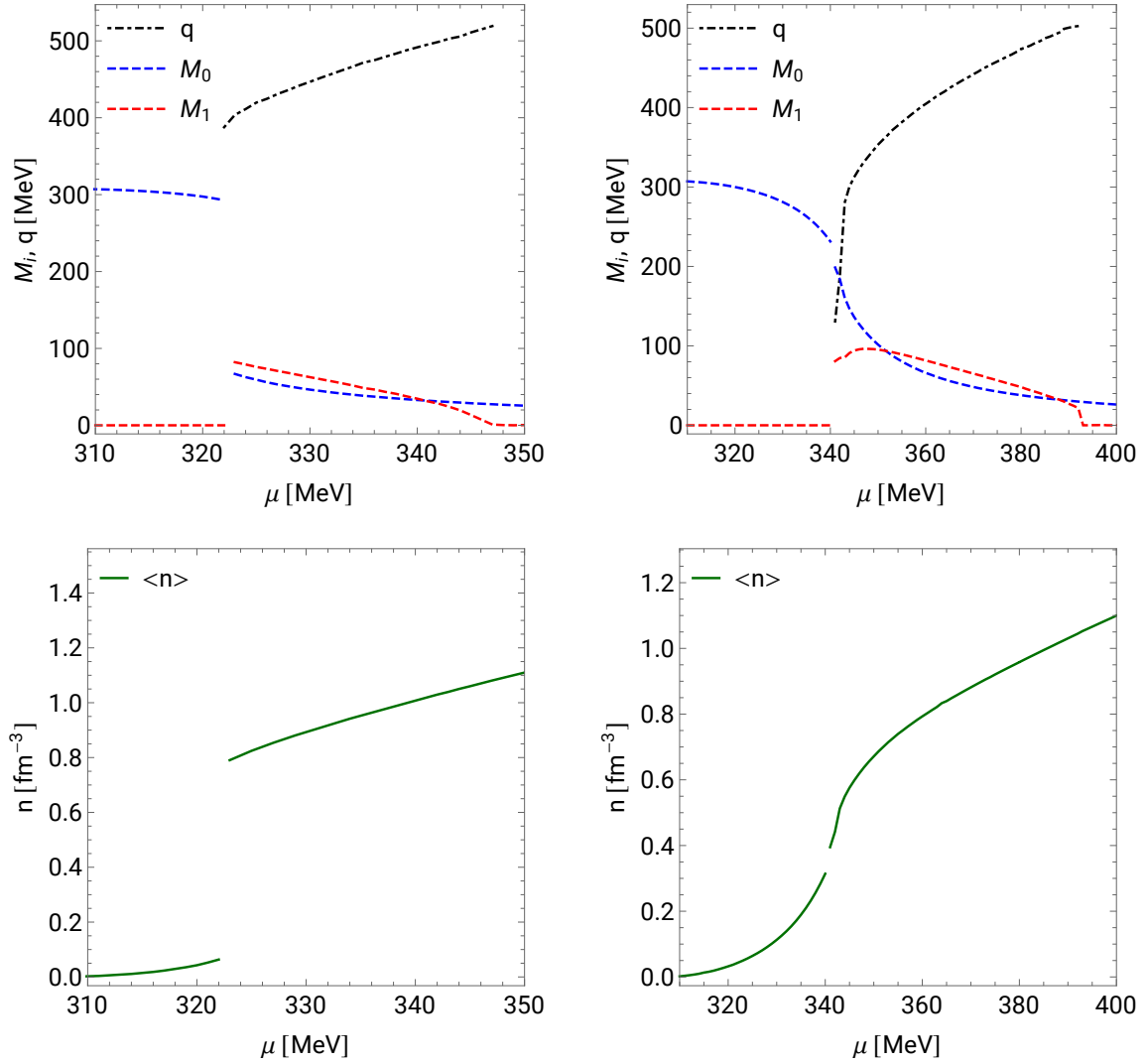
Figure 6.5.: M_i, q (top) and average density (bottom) plotted against μ for the M_0-shifted chiral density wave (CDW+) in ADA for $g_v/g_s = 0.0$ (left) and $g_v/g_s = 0.3$ (right) with $m = 5\,\mathrm{MeV}$.

6.2.2. Density

Up to now, we performed the calculations with non-vanishing m in ADA. Now we include the space-dependent part of the density to investigate if the density of the CDW is still homogeneous as in the chiral limit. In figure 6.6 the thermodynamic potential in the direction of the density amplitude n_A is shown for $g_v/g_s = 0.3$. To reduce the computation time we derived each point by fixing q, M_1 and $\tilde{\mu}_0$ to the solution in ADA. We immediately see that breaking the chiral symmetry explicitly leads to a small but non-vanishing space-depending contribution. If we had minimized and maximized w.r.t. the stated parameters the maximum would be somehow shifted from the current position but it would nevertheless differ from zero.
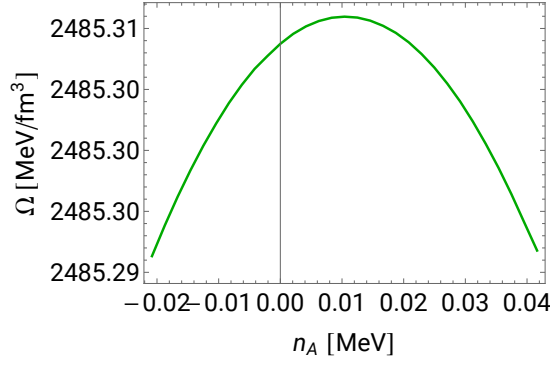
Figure 6.6.: Thermodynamic potential in n_A-direction for $g_v/g_s = 0.3$ and $m = 5\,\mathrm{MeV}$ at $\mu = 345\,\mathrm{MeV}$. The values for q, M_0, M_1 and $\tilde{\mu}_0$ were fixed to the solution in ADA.

6.3. Cosine

For the cosine+ in ADA, a similar behavior as for the CDW+ can be observed, see figure 6.7. The modulation momentum and the average density in the beginning of the inhomogeneous phase are strongly suppressed by the vector interaction and the first order transition is weakened. Due to numerical difficulties we have a gap between $\mu = 340\,\mathrm{MeV}$ and $\mu = 341\,\mathrm{MeV}$. In the beginning of the inhomogeneous phase, M_0 is twice as large as M_1 and the latter one increases slightly until they cross each other and decline together until M_1 drops to zero by a second order transition.

6.4. Higher coefficients

Now we include higher coefficients, $M_{\pm 2}$ and $M_{\pm 3}$. The 'minus' coefficients are set to $M_{-2} = M_2$ and $M_{-3} = M_3$ to obtain real solutions:

$$M_7(z) = M_0 + 2M_1 \cos(qz) + 2M_2 \cos(2qz) + 2M_3 \cos(3qz). \tag{6.1}$$

In the chiral limit, all even Fourier coefficients vanish since the Jacobi elliptic functions are the most favored solutions and can be expressed as

$$M_{\mathrm{soli}}(z) = \sum_{n>0,\ \mathrm{odd}} M_n \sin(nqz). \tag{6.2}$$

With explicitly broken chiral symmetry the even coefficients generally do not vanish, as we can see in figure 6.8 (left). Comparing the left and right picture of figure 6.8 we see immediately that M_2 has an even larger contribution than M_3. In contrast to M_0 and M_1 the higher coefficients only have negative solutions. In figure 6.9 the Fourier coefficients and q are plotted against the chemical potential for $g_v/g_s = 0.0$ (left) and $g_v/g_s = 0.3$ (right). For $g_v/g_s = 0.0$ the M_2 adds a negative minor contribution just at the vicinity of the first order transition and M_3 is practically zero. For $g_v/g_s = 0.3$ they have a stronger and longer contribution. M_3 becomes negligible quite prompt and M_2 contributes nearly up to the middle of the inhomogeneous phase until it vanishes approximately. The modulation momentum is suppressed by the vector interactions but its slope in the beginning of the inhomogeneous phase is not as strong as for the CDW+ and cosine+.
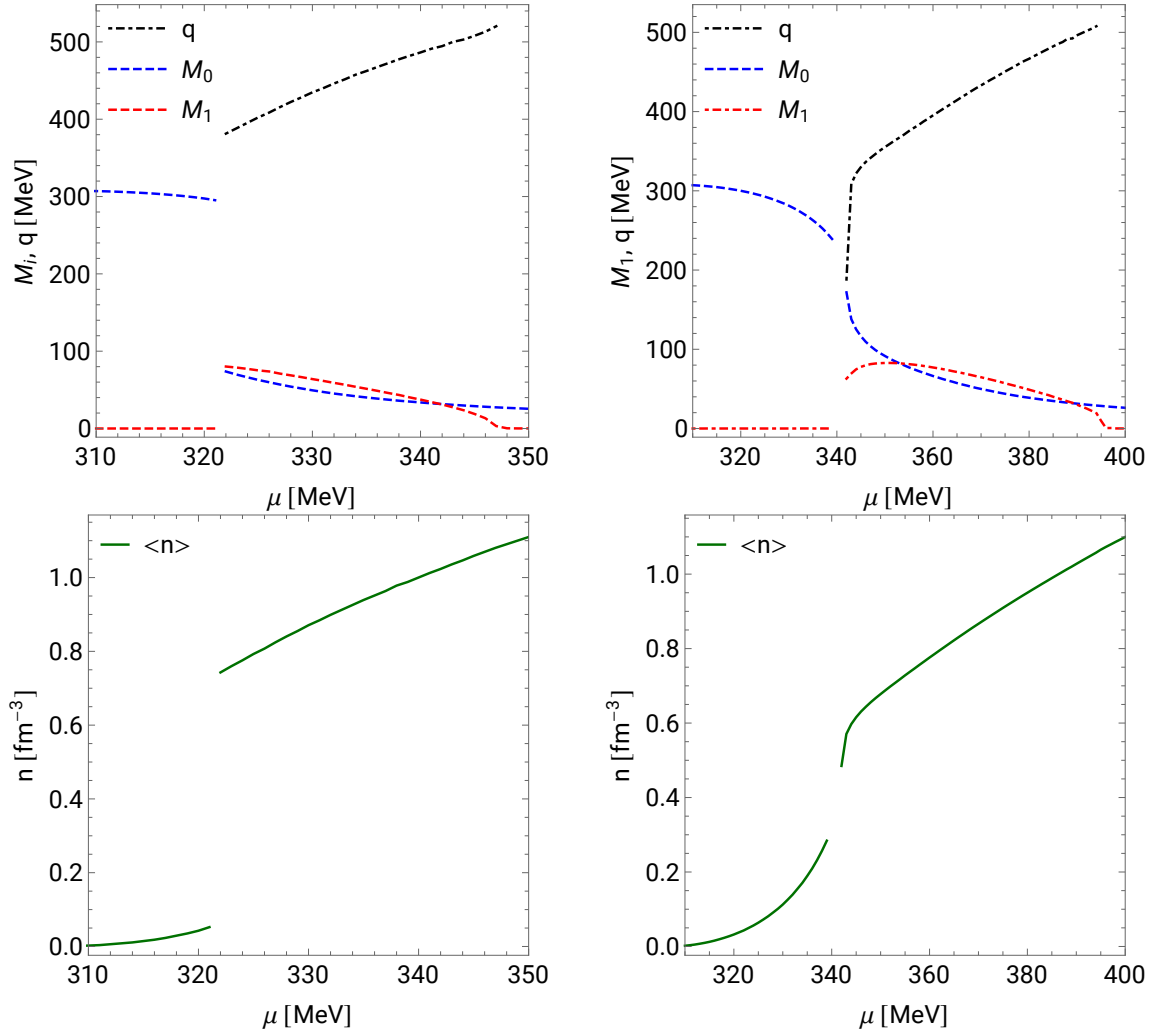
Figure 6.7.: M_i, q (top) and homogeneous density (bottom) plotted against μ for the cosine with constant shift for $g_v/g_s = 0.0$ (left) and $g_v/g_s = 0.3$ (right) with $m = 5\,\mathrm{MeV}$.

6.5. Solitonic solution

6.5.1. General

Here, we will investigate the solitonic solution only for $g_v/g_s = 0.0$. In the chiral limit, it is the most favored solution so far. This is not known for the case of a non-vanishing m. The solitons with finite current quark mass are given by [40]

$$M(z) = \Delta \left(\nu\, \mathrm{sn}(b|\nu)\mathrm{sn}(\Delta z|\nu)\mathrm{sn}(\Delta z + b|\nu) + \frac{\mathrm{cn}(b|\nu)\mathrm{dn}(b|\nu)}{\mathrm{sn}(b|\nu)} \right) \tag{6.3}$$

where we get an additional parameter b, the parameters Δ and ν were already introduced in section 4.2. Due to periodicity the parameters b and ν can be limited to $b \in [0, \mathbf{K}(\nu)]$, with the complete elliptic integral of the first kind $\mathbf{K}$. Only the first term gives a space-dependency to the ansatz while the second term gives
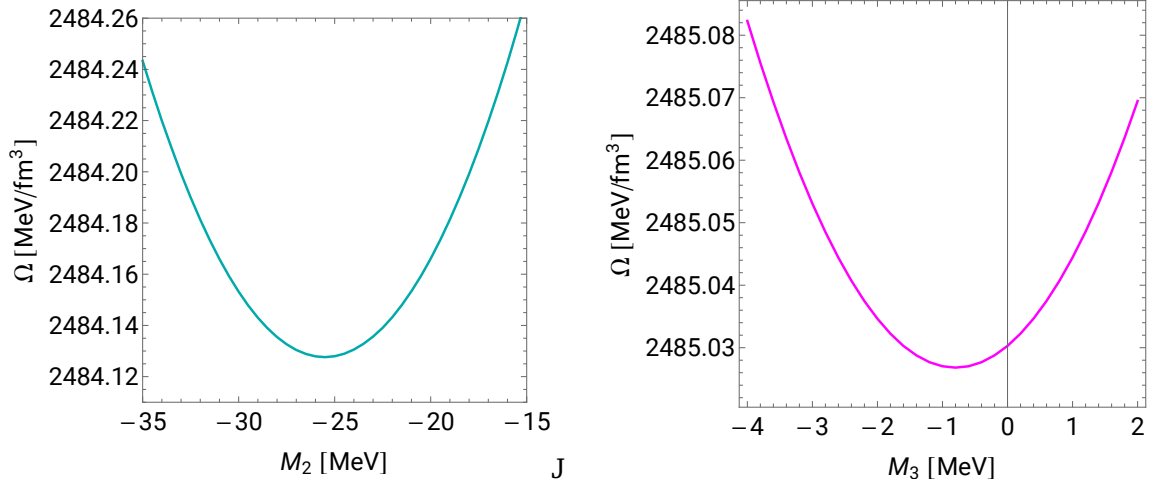
Figure 6.8.: Thermodynamic potential in M_2- (left) and M_3-direction (right) for $g_v/g_s = 0.3$, $m = 5\,\text{MeV}$ and $\mu = 345\,\text{MeV}$. For each point the thermodynamic potential was minimized w.r.t. q, M_0 and M_1 and maximized w.r.t. $\tilde{\mu}_0$.
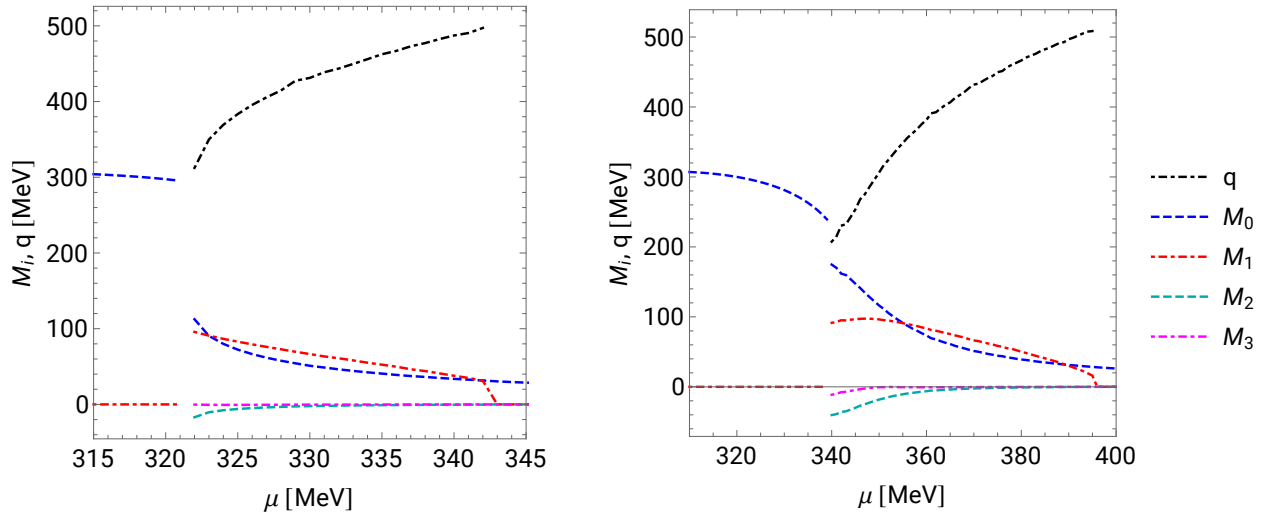
Figure 6.9.: M_i and q plotted for the 7-coefficient ansatz, for $g_v/g_s = 0.0$ (left) and $g_v/g_s = 0.3$ (right) both with $m = 5\,\text{MeV}$. The 'minus' coefficients of the spatially dependent part of equation (6.1) were set to $M_{-i} = M_i$.

a constant shift. The chiral limit corresponds to $b = \mathbf{K}(\nu)$. The distribution of the eigenvalues λ gets shifted by

$$\lambda \longrightarrow \text{sgn}(\lambda)\sqrt{\lambda^2 + \delta\Delta^2} \tag{6.4}$$

$$\text{with} \quad \delta = \frac{1}{\text{sn}^2(b|\nu)} - 1 \geq 0. \tag{6.5}$$

For numerical reasons, it is practical to express the mass ansatz as a function of δ instead of b, so it can be

rewritten into

$$M(z) = \frac{\Delta}{\sqrt{1+\delta}} \left(\nu \, \text{sn}(\Delta z | \nu) \text{sn}(\Delta z + b(\delta) | \nu) + (1+\delta) \, \text{cn}(b(\delta) | \nu) \text{dn}(b(\delta) | \nu) \right) \tag{6.6}$$

with

$$b = \text{sn}^{-1} \left(\left. \frac{1}{\sqrt{1+\delta}} \right| \nu \right) . \tag{6.7}$$

For an elliptic modulus of $\nu = 1$ equation (6.6) results in

$$M(z) = \frac{\Delta}{\sqrt{1+\delta}} \left(\nu \, \delta + \tanh(z\Delta) \tanh\left(z\Delta + \text{artanh}\left(\frac{1}{\sqrt{1+\delta}} \right) \right) \right) . \tag{6.8}$$

and therefore forms a 'single kink' (single soliton). Compared to the chiral limit, the single kink is deformed and shifted. If the elliptic modulus is set to $\nu = 0$ equation (6.6) results in a constant function

$$M(z) = \Delta \sqrt{\delta} . \tag{6.9}$$

Both cases are shown in figure 6.10.
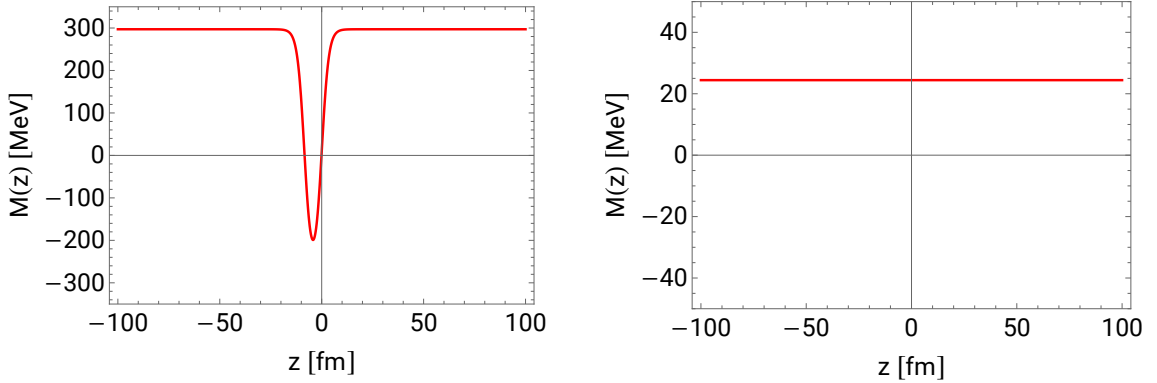
Figure 6.10.: Solitonic solutions for $\mu = 320 \, \text{MeV}$ (left) and $\mu = 350 \, \text{MeV}$ (right), for $g_v/g_s = 0.0$ and $m = 5 \, \text{MeV}$. The values for the parameters Δ, ν and δ in the thermodynamic equilibrium at the corresponding chemical potentials are given by $(\Delta, \, \nu, \, \delta) = (293.0, \, 1.0, \, 0.028)$ (left) and $(\Delta, \, \nu, \, \delta) = (87.8, \, 0.0, \, 0.008)$ (right).

The thermodynamic potential [25] for $T = 0$ can be expressed as

$$\Omega(\mu; \Delta, \nu, \delta) = -N_f N_c \int_0^\infty dE \, \tilde{\rho}(E) \tilde{f}\left(\sqrt{E^2 + \delta \Delta^2} \right) + \frac{1}{l(\Delta, \nu)} \int_0^{l(\Delta, \nu)} dz \frac{|M(z) - m|^2}{4g_s} \tag{6.10}$$

where the density of states $\tilde{\rho}(E)$ can be derived analytically and is given by [25]

$$\tilde{\rho}(E) = \frac{E\Delta}{\pi^2} \left\{ \Theta\left[\sqrt{\tilde{\nu}}\Delta - E\right] \left(\mathbf{E}(\tilde{\Theta}|\tilde{\nu}) + \left(\frac{\mathbf{E}(\nu)}{\mathbf{K}(\nu)} - 1\right) \mathbf{F}(\tilde{\Theta}|\tilde{\nu})\right) \right.$$
$$+ \Theta\left[E - \sqrt{\tilde{\nu}}\Delta\right] \Theta\left[\Delta - E\right] \left(\mathbf{E}(\tilde{\nu}) + \left(\frac{\mathbf{E}(\nu)}{\mathbf{K}(\nu)} - 1\right) \mathbf{F}(\tilde{\Theta}|\tilde{\nu})\right)$$
$$\left. + \Theta\left[E - \Delta\right] \left(\mathbf{E}(\Theta|\tilde{\nu}) + \left(\frac{\mathbf{E}(\nu)}{\mathbf{K}(\nu)} - 1\right) \mathbf{F}(\Theta|\tilde{\nu}) + \sqrt{(E^2 - \Delta^2)(E^2 - \tilde{\nu}\Delta^2)}/(E\Delta)\right) \right\}. \tag{6.11}$$

$l(\Delta, \nu) = \dfrac{2\mathbf{K}(\nu)}{\Delta}$ is the period of the modulation, $\mathbf{F}$, $\mathbf{E}$ and $\mathbf{K}$ are the elliptic integrals of the first and second kind. We defined $\tilde{\nu} = 1 - \nu$, $\tilde{\Theta} = \arcsin\left(E/(\sqrt{\tilde{\nu}}\Delta)\right)$, $\Theta = \arcsin(\Delta/E)$ as well as

$$\tilde{f}(x) = \tilde{f}_{\text{vac}}(x) + \tilde{f}_{\text{med}}(x) \tag{6.12}$$
$$\tilde{f}_{\text{vac}}(x) = x \tag{6.13}$$
$$\tilde{f}_{\text{med}}(x) = (\mu - x)\Theta\left[\mu - x\right]. \tag{6.14}$$

The vacuum term is the only divergent part and gets Pauli-Villars regularized. With the expression of the thermodynamic potential as a function of Δ, ν and δ we can perform our investigations by minimizing the potential with respect to these parameters.

6.5.2. Numerical results

The results of the numerical calculations for the parameters Δ, ν and δ against μ are shown in figure 6.11. The lower right panel shows the amplitudes of the constant M_{const}, the prefactor M of the space-dependent part and the total M_{total} of the mass function as well as the wavenumber q given by

$$M_{\text{const}} = \Delta\sqrt{1 + \delta}\, \text{cn}(b(\delta)|\nu)\text{dn}(b(\delta)|\nu) \tag{6.15}$$
$$M = \frac{\Delta\nu}{\sqrt{1 + \delta}} \tag{6.16}$$
$$M_{\text{total}} = M_{\text{const}} + M \tag{6.17}$$
$$q = \frac{2\pi}{l(\Delta, \nu)} = \frac{\pi\Delta}{\mathbf{K}(\nu)}. \tag{6.18}$$

The first homogeneous phase is characterized by $\nu = 1$, and due to equation (6.18) by a vanishing q, just as in the chiral limit. As a result, the solitons have an infinite periodicity causing the single kink as in figure 6.10. The distinction between M and M_{const} becomes meaningless since both terms of equation (6.6) become constant, so only M_{total} is considered. M_{total} exhibits constant progress initially and starts to decrease slightly from a certain chemical potential. At the left phase boundary, the inhomogeneous phase is initialized by a second order transition of ν. This leads to a second order transition of q from zero to non-zero values. Δ and δ are not shown in the homogeneous phases, this will be discussed shortly. M_{total} exhibits a second order transition to the inhomogeneous phase, too. In the inhomogeneous window, Δ only varies in a small region between 275–$290\,\text{MeV}$ while δ decreases by a factor of 5. The corresponding
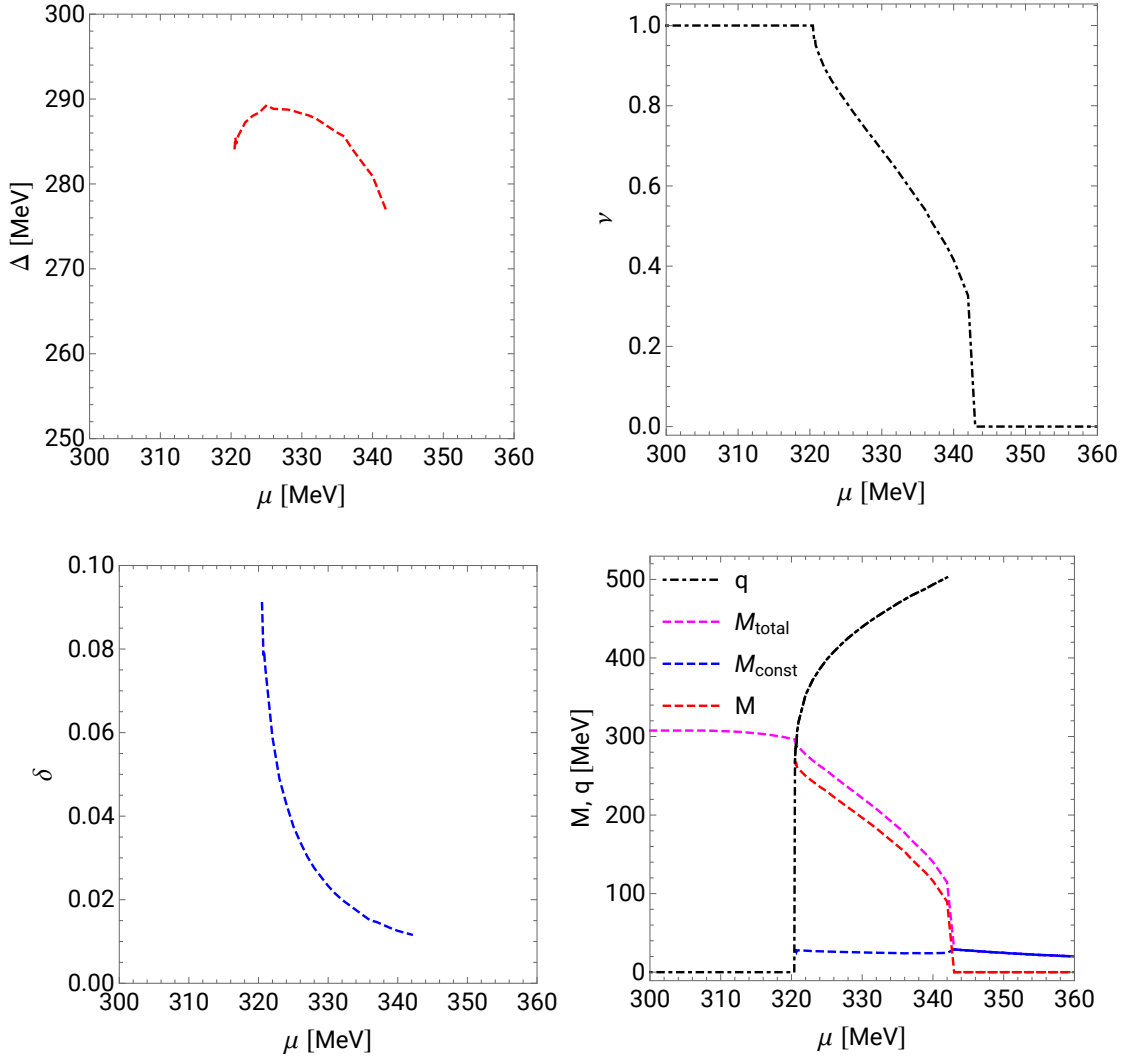
Figure 6.11.: Δ, ν, δ, M_i and q against μ for $g_v/g_s = 0.0$ and $m = 5\,\text{MeV}$.

curves in figure 6.11 show little kinks which is due to the numerics. At the right phase boundary, the second homogeneous phase starts by a second order transition of ν. The second homogeneous phase is characterized by a vanishing ν. As a result, M vanishes by a second order transition. q is not shown here since it is an unphysical quantity when M vanishes. M_{const} remains non-zero but it rises to a slightly higher value from about $24\,\text{MeV}$ to $27\,\text{MeV}$, actually we expect M_{const} to be smooth.

The results for Δ and δ in the homogeneous phases are ambiguous since the thermodynamic potentials in the Δ-δ-plane exhibit degenerated minima. So the parameters are not shown in the homogeneous phases in figure 6.11. The thermodynamic potential in both the first and second homogeneous phase are shown in figure 6.12 for $\mu = 320\,\text{MeV}$ and $\mu = 345\,\text{MeV}$, respectively, where the degenerated minima are marked by the black lines. The parameters adjust themselves appropriately so that the values for M_{total} in figure 6.11 stay the same for the respective μ. The Δ-δ-plane for $\mu = 320\,\text{MeV}$ exhibits degenerated minima at smaller values of Δ too, but these solutions are not energetically favored.

The thermodynamic potentials in Δ, ν and δ-direction, respectively, in the inhomogeneous phase for $\mu = 325\,\text{MeV}$ and $\mu = 340\,\text{MeV}$ are shown in figure 6.13. For each point, the thermodynamic potentials were
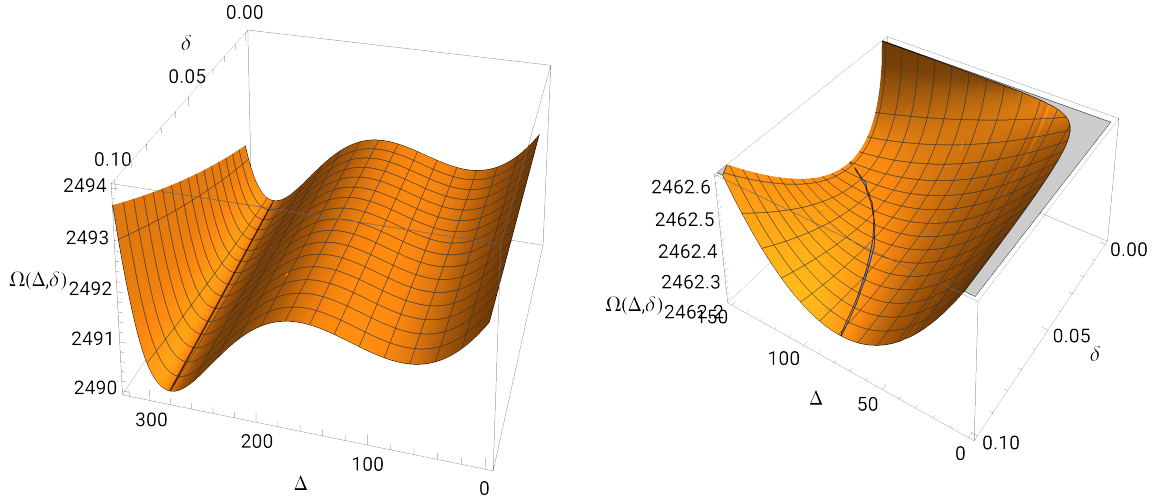
Figure 6.12.: Δ-δ-plane for $\mu = 320\,\mathrm{MeV}$ and $\nu = 1.0$ (left) and for $\mu = 345\,\mathrm{MeV}$ and $\nu = 0.0$ (right) for $g_v/g_s = 0.0$ and $m = 5\,\mathrm{MeV}$.

minimized w.r.t. the remaining parameters. Δ exhibits two minima in the beginning of the inhomogeneous phase. The energetically higher minimum dissipates with rising μ. The thermodynamic potential in ν-direction shows two extrema in the whole inhomogeneous window from which the global minimum shifts to smaller values of ν. At both $\mu = 325\,\mathrm{MeV}$ and $\mu = 345\,\mathrm{MeV}$ the extrema at $\nu = 0$ seem to be weakly pronounced minima, but due to the numerics is cannot be excluded that they are maxima. The thermodynamic potential in δ-direction exhibits only one extremum which is the global minimum. As figure 6.11 already indicated, the global minimum in Δ-direction just changes slightly. In contrast, the global minima of ν and δ shifts to smaller values significantly.

With the solutions in the thermodynamic equilibrium, we can compare the mass ansatz of the solitons with the 7-coefficient Fourier ansatz given by equation (6.1). Afterward, we will derive the first lower Fourier coefficients of the solitonic solution explicitly. For the comparison of the mass ansätze of equation (6.3) and equation (6.1) the functions are shown in figure 6.14 for $\mu = \{325, 335, 342\}\mathrm{MeV}$. The values of the corresponding parameters of both ansätze in the thermodynamic equilibrium are given by:

	Solitons			7-coefficient Fourier ansatz				
μ [MeV]	Δ [MeV]	ν	δ	q [MeV]	M_0 [MeV]	M_1 [MeV]	M_2 [MeV]	M_3 [MeV]
325	289.26	0.81055	0.03760	398.504	65.029	79.364	-4.578	-0.527
335	286.05	0.56639	0.01631	469.152	38.196	48.118	-0.787	-0.127
342	276.73	0.32668	0.01164	502.032	30.121	25.053	-0.116	-0.019

Table 6.1.: Results of the parameters Δ, ν and δ of the solitonic solution and q as well as the Fourier coefficients of the 7-coefficient Fourier ansatz for several chemical potentials in the thermodynamic equilibrium. The values for q and M_n are given by the results of figure 6.9.

As we can see in figure 6.14, the solitonic modulation coincides well with the 7-coefficient Fourier ansatz in the whole inhomogeneous region. Only in the beginning, e.g. at $\mu = 325\,\mathrm{MeV}$, they show slight differences.
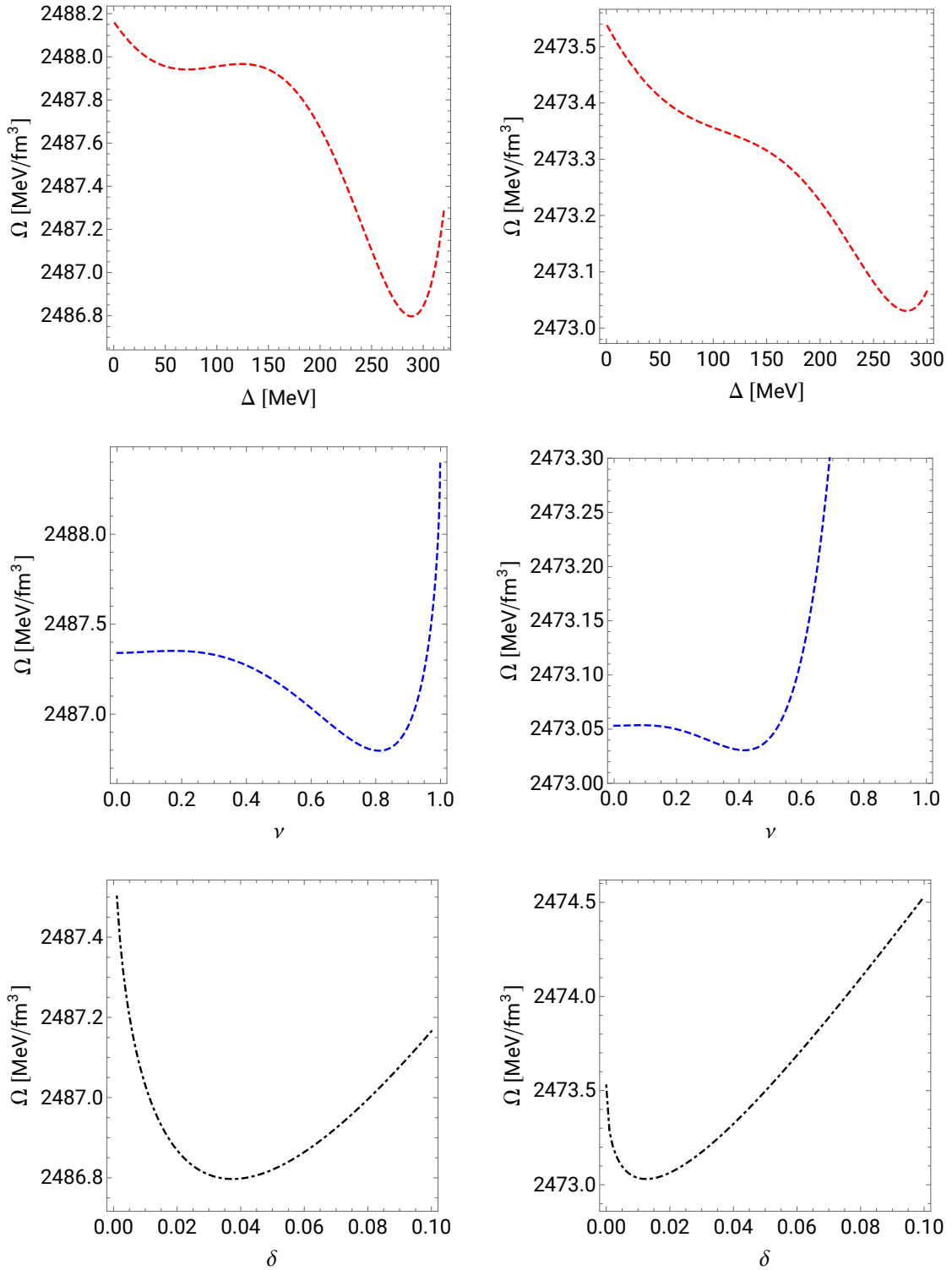
Figure 6.13.: Thermodynamic potentials in Δ, ν and δ-direction (from top to bottom) for $g_v/g_s = 0.0$ and $m = 5\,\mathrm{MeV}$, for $\mu = 325\,\mathrm{MeV}$ (left) and $\mu = 340\,\mathrm{MeV}$ (right). For each point the thermodynamic potentials were minimized w.r.t. the remaining parameters.
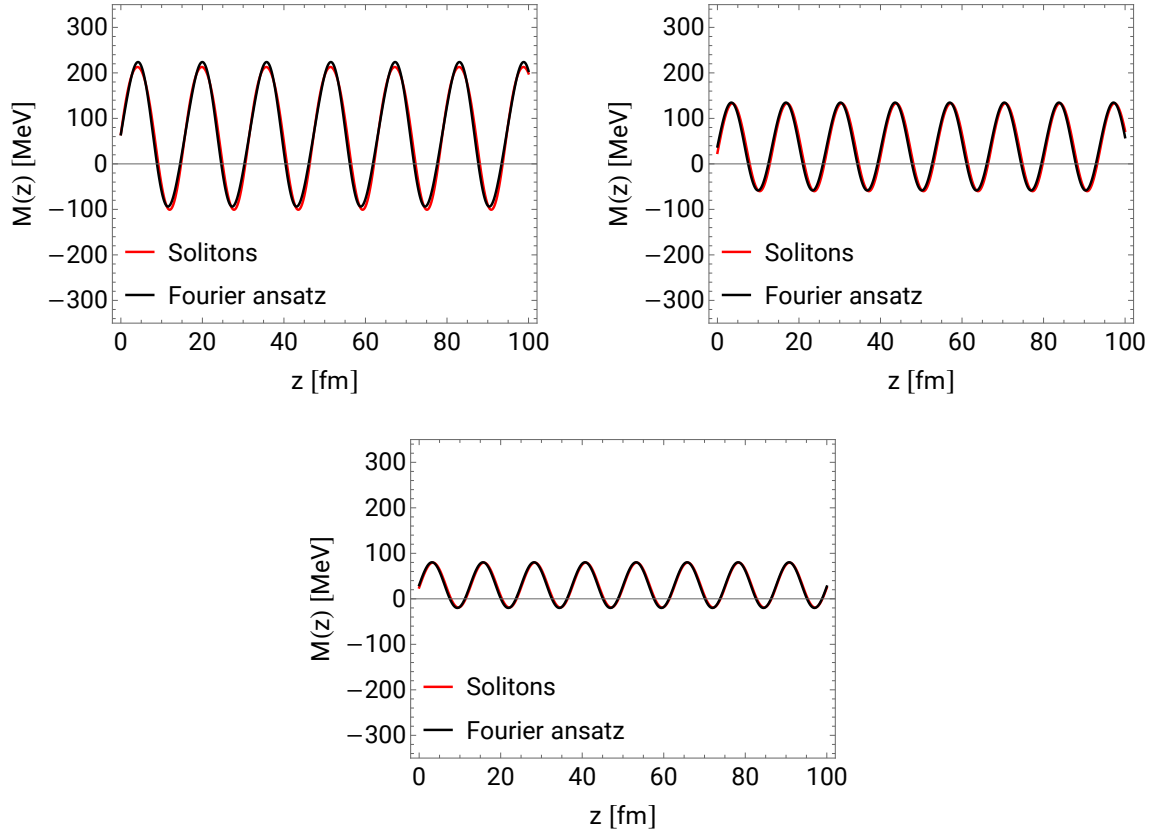
Figure 6.14.: Comparison of the solitonic and the 7-coefficient Fourier modulation with the parameters of table 6.1 for $\mu = 325\,\mathrm{MeV}$ (top left), $335\,\mathrm{MeV}$ (top right) and $342\,\mathrm{MeV}$ (bottom) for $g_v/g_s = 0.0$ and $m = 5\,\mathrm{MeV}$.

The next step is to derive the first lower coefficients of the solitonic solutions explicitly. Therefor, we compose them in a Fourier series. The Fourier coefficients M_n can be derived by

$$M_n = \frac{1}{l(\Delta, \nu)} \int\limits_0^{l(\Delta, \nu)} M(z) \exp\left(in \frac{2\pi}{l(\Delta, \nu)} z\right). \tag{6.19}$$

The results of the first nine coefficients are listed in table 6.2.

As we can see the Fourier coefficients, except M_0, are complex-valued but the $M_{\pm n}$-pairs are complex conjugated to each other. In total, this gives a real solution, a sum of sines and cosines

$$M(z) = \sum_{n \geq 0} \left(\mathcal{M}_n \cos(nqz) + \mathcal{N}_n \sin(nqz)\right) \tag{6.20}$$

with

$$\mathcal{M}_n = 2\Re(M_n) \tag{6.21}$$
$$\mathcal{N}_n = 2\Im(M_n^*). \tag{6.22}$$

μ	M_0	M_1	M_{-1}	M_2	M_{-2}
325	65.264601	$-11.498071 - 37.762443i$	M_1^*	$1.937254 - 1.300276i$	M_2^*
335	38.095494	$-3.797482 - 23.884291i$	M_1^*	$0.374718 - 0.122247i$	M_2^*
342	30.544021	$-1.480971 - 12.242472i$	M_1^*	$0.071010 - 0.017435i$	M_2^*

M_3	M_{-3}	M_4	M_{-4}
$-0.210202 - 0.171412i$	M_3^*	$0.015426 - 0.037687$	M_4^*
$-0.026820 - 0.052406i$	M_3^*	$0.001639 - 0.001197i$	M_4^*
$-0.002504 - 0.006629i$	M_3^*	$0.000077 - 0.000040i$	M_4^*

Table 6.2.: First nine coefficients of the Fourier decomposition of equation (6.6) for several chemical potentials. All quantities are given in MeV.

The coefficients $\mathcal{M}_n$ and $\mathcal{N}_n$ of equation (6.20) from $n = 1$ to $n = 4$ are given by:

μ	$\mathcal{M}_1$	$\mathcal{N}_1$	$\mathcal{M}_2$	$\mathcal{N}_2$	$\mathcal{M}_3$	$\mathcal{N}_3$	$\mathcal{M}_4$	$\mathcal{N}_4$
325	-22.996142	75.524885	3.874507	2.600552	-0.420403	0.342824	0.0308538	0.075374
335	-7.594965	47.768582	0.749437	0.244494	-0.053640	0.104811	0.003278	0.002393
342	-2.961942	24.484945	0.142019	0.034870	-0.005008	0.013257	0.000154	0.000080

Table 6.3.: First coefficients, from $n = 1$ to $n = 4$ of equation (6.20) for several chemical potentials. All quantities are given in MeV.

The signs of $\mathcal{M}_n$ alternate with rising n while $\mathcal{N}_n$ are positive. $\mathcal{N}_1$ has the largest contribution, so the sine with $n = 1$ provides the dominating term. This domination increases with rising chemical potential and becomes clear by comparing the coefficients with $\mathcal{N}_1$. This comparison is shown in table 6.4. As a result, the solitons can be well approximated by the sine from the middle of the inhomogeneous phase.

μ [MeV]	$\mathcal{M}_1/\mathcal{N}_1$	$\mathcal{N}_2/\mathcal{N}_1$	$\mathcal{M}_2/\mathcal{N}_1$	$\mathcal{N}_3/\mathcal{N}_1$	$\mathcal{M}_3/\mathcal{N}_1$	$\mathcal{N}_4/\mathcal{N}_1$	$\mathcal{M}_4/\mathcal{N}_1$
325	-0.304484	0.034433	0.051301	0.004539	-0.005566	0.000998	0.000409
335	-0.158995	0.005118	0.015689	0.002194	-0.001123	0.000048	0.000069
342	-0.120970	0.001424	0.005800	0.000542	-0.000205	0.000006	0.000003

Table 6.4.: Ratios of the coefficients of table 6.3 compared to $\mathcal{N}_1$.

6.6. Free energies

The free energies for the homogeneous solution, CDW+, cosine+ and 7-coefficients in ADA for $g_v/g_s = 0.0$ (left) and $g_v/g_s = 0.3$ (right) are shown in figure 6.15. Additionally, in the left panel, the free energy of the solitonic solution is shown. The free energies are plotted with respect to a hypothetical restored phase. Just

as in the chiral limit complex solutions are always disfavored against real modulations and including higher Fourier coefficients leads to a gain in free energy. In both cases of g_v/g_s the 7-coefficient ansatz is almost degenerate with the (shifted) cosine from the middle of the inhomogeneous phase while the (shifted) CDW only coincides both solutions at the second order phase boundary at the upper end of the inhomogeneous phase. For $g_v/g_s = 0.0$ the solitons are most favored and coincide with the 7-coefficient ansatz in the whole inhomogeneous phase. It should be noted that it is not known if the solitons are the most favored solutions in general. At the left phase boundary in both pictures of figure 6.15 the free energies of the cosine and 7-coefficient ansatz show strong kinks, this is due to numerical artifacts.
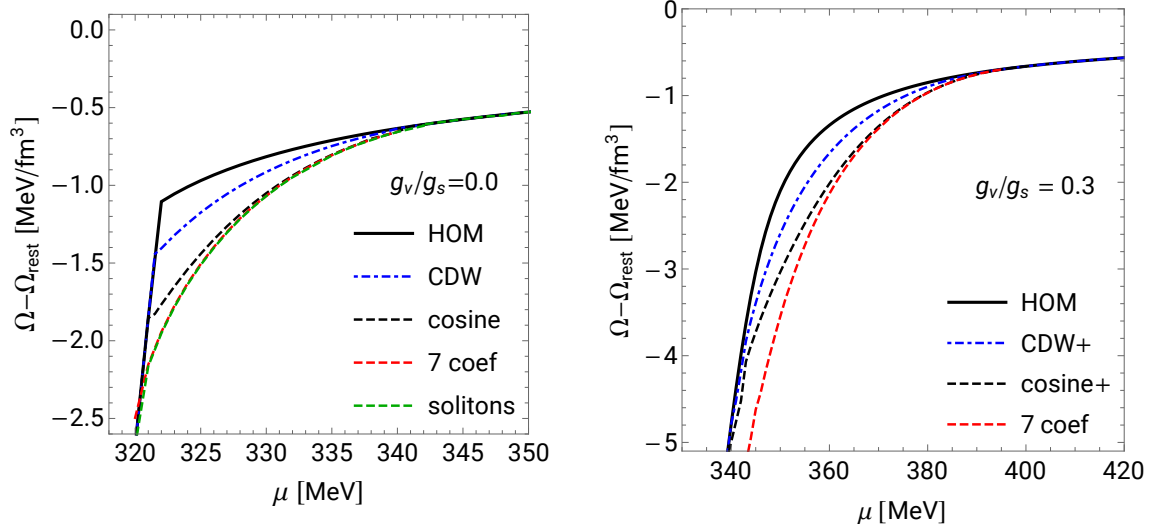

Figure 6.15.: Free energies for the homogeneous solution, CDW+, cosine+ and 7-coefficient ansatz in ADA for $g_v/g_s = 0.0$ (left) and $g_v/g_s = 0.3$ (right) for $m = 5\,\mathrm{MeV}$. Additionally, in the l.h.s. the free energy of the solitons is shown.

7. Conclusion and outlook

In this thesis, the inhomogeneous phases with vanishing and finite current quark mass in the vector interaction extended Nambu-Jona-Lasinio model were investigated. The Lagrangian of the NJL model with vector interactions was introduced and a mean-field approximation was performed, where periodic modulations in space were allowed. The corresponding Hamiltonian was transformed into momentum space by using a Fourier expansion for the condensates. Since the Hamiltonian matrix is infinite in momentum space, a numerical cutoff was applied to restrict the momentum space. Furthermore, the Bloch theorem was applied and for constant and vanishing vector condensates the Lorentz symmetry of the system was taken into advantage to simplify the matrix structure. By doing this, a general expression for lower d-dimensional modulations could be obtained, from which one-dimensional modulations with and without vector interactions, that is for $g_v \neq 0$ or $g_v = 0$ respectively, could be investigated. The occurring integrals were rendered finite with the Pauli-Villars regularization. To further simplify the numerical calculations for large momenta, the asymptotic behavior of the integrand of the thermodynamic potential was utilized and the eigenvalues were approximated by the homogeneous eigenvalues which can be derived analytically.

For the calculations in thermodynamic equilibrium, we used a minimizing routine, by which the potential was minimized with respect to M_n and q and maximized with respect to $\tilde{\mu}_n$. In the chiral limit, we briefly discussed the findings of previous works for several vector couplings by regarding the chiral density wave and sinusoidal modulations and investigated the thermodynamic potential to get a deeper understanding of these findings. For the investigations, the potential was plotted in the plane or direction of the relevant coefficients and minimized with respect to q and the remaining coefficients of the mass and shifted chemical potential ansatz. For vanishing vector interactions we found that the chiral density wave occupies a saddle point in the M_1-M_{-1}-plane where it has a maximum in M_{-1}-direction at $M_{-1} = 0$, M_0 vanished trivially for all one-dimensional modulations. So although the CDW is a self-consistent solution in the chiral limit, it is not a stable solution. The cosine occupies the global minimum and thus, it is energetically favored. With non-vanishing vector interactions we applied a homogeneous density ansatz and spatially modulated density ansatz to the CDW and cosine, respectively. The CDW is known to have a homogeneous density, we could confirm this by finding a vanishing density amplitude. The case of $g_v/g_s = 0.3$ was of particular interest since there is a region where the CDW is favored, up to a certain chemical potential where the cosine is favored. In the region where the CDW is favored the potential exhibits two minima, one of the favored CDW at more favorable energies and one of the cosine with spatially modulated density. With rising chemical potential the free-energy difference in the two minima changes until the minimum of the cosine lies at more favorable energies and the minimum of the CDW turns into a maximum.

By breaking the chiral symmetry explicitly with a bare quark mass of $m = 5\,\mathrm{MeV}$ we found for the homogeneous case that the vector interactions weaken the first order transitions, so the first order transition turns into a crossover. The investigation of the thermodynamic potential in the M_{-1}-M_0-plane shows that the CDW exhibits a maximum with respect to M_{-1} but not an extremum regarding M_0. On the other hand, moving into the minimum w.r.t. M_0 shows the absence of an extremum regarding M_{-1}. These observations demonstrate the non-self-consistency of the CDW. Comparing the free energies of the

homogeneous solution for several bare quark masses with the CDW exhibits a border of $m \approx 3\,\mathrm{MeV}$ where the homogeneous solution is favored against the CDW, so it is meaningful to extend the CDW by M_0, nevertheless. Also, the cosine was extended by M_0 since the broken chiral symmetry yields a non-trivial M_0. For the one-dimensional modulations, the vector interactions weaken the first order transition too so in the beginning of the inhomogeneous phase q drops to quite small values $< 200\,\mathrm{MeV}$ and exhibits a large slope. Also, the quark number density gets suppressed. The suppression of the first order transition gives rise to suggestions if the vector interactions could change the transition to a nearly second order transition. Since the numerical derivations fail due to the large matrix size for $q < 150\,\mathrm{MeV}$ it should be examined if the eigenvalues of the CDW, shifted by a constant, can be derived analytically which is, as least, possible in the chiral limit. Including higher coefficients leads to a gain in the free energy, and the contribution of the higher coefficients get amplified by vector interactions.

For the case of explicitly broken chiral symmetry, the solitonic solution was only considered with vanishing vector interactions. In contrast to the chiral limit case, the mass ansatz is modified, including an additional parameter b with respect to which the thermodynamic potential has to be minimized. As a result of the modified mass ansatz, the single kink in the case of $\nu = 1$ is shifted and deformed compared to the chiral limit case. Also for $\nu = 0$, where the mass function is constant, is shifted from zero. In both homogeneous phases, we receive ambiguous solutions for the parameters Δ and δ since the thermodynamic potentials provide degenerated minima in the Δ-δ-plane. At the left phase boundary, we find a second order transition of ν and consequently of both the total of the mass function M_{total} and the wavenumber q, as we would find it in the chiral limit. In the second homogeneous phase the prefactor M of the space-dependent part vanishes so M_{total} coincides with the constant M_{const}. But, contrary to expectations, at the right phase boundary M_{const} did not perform a smooth transition between the phases but changes from about $24\,\mathrm{MeV}$ to $27\,\mathrm{MeV}$. There was not enough time to examine the reason for this issue. One option would be to calculate the thermodynamic potential in the Δ-δ-plane and minimize w.r.t. ν on the left and right of the right phase boundary in order to check if the minimizing routine gave correct results. By comparing the solitonic and the 7-coefficient Fourier modulation for several μ we find that the modulations coincide well in the whole inhomogeneous window. The Fourier coefficients of the solitons are complex-valued where the $M_{\pm n}$-pairs are complex conjugated to each other. Due to that, the Fourier decomposition can be composed into a sum of sines and cosines where the coefficients are related to the real and imaginary parts of the Fourier coefficients. By comparing the coefficients of the sines and cosines we find the contribution of the sine for $n = 1$ to be dominating. This domination rises with increasing chemical potential. As a result, the solitons can be well approximated by the sine from the middle of the inhomogeneous phase.

The next step would be to consider explicitly broken chiral symmetry with spatially modulated vector condensates. Especially since the density of the CDW turns out not to be homogeneous this would be an interesting task. It should be investigated if the CDW is still favored against the cosine with spatially modulated density at large g_v/g_s. To simplify the numerical calculations it would be helpful to find a boosting procedure as it was not possible to derive an expression analogous to the $g_v/g_s = 0$ or ADA case. Further work is necessary with regard to the solitonic solutions. Our investigations were restricted to $g_v/g_s = 0$ and the next step should be to consider $g_v/g_s \neq 0$ in ADA and thereafter with spatially modulated vector condensates. Since the Fourier coefficients of the solitonic solution is complex-valued future works could investigate lower Fourier ansätze with complex-valued coefficients. If the $M_{\pm n}$-pairs are taken as complex conjugated to each other the resulting Hamiltonian matrix is still hermitian.

A. Appendix

A.1. Conventions

In this thesis natural units are used, that is

$$\hbar = k_B = c = 1. \tag{A.1}$$

To reconstruct the proper units of the thermodynamic potential, that is $\mathrm{MeV\,fm}^{-3}$, the result has to be multiplied by $(\hbar c)^{-3} = (197\,\mathrm{MeV\,fm})^{-3}$.

The convention of the Minkowski metric is

$$(\eta)_{\mu,\nu} = \mathrm{diag}(1, -1, -1, -1). \tag{A.2}$$

The gamma matrices are used in the chiral representation

$$\gamma^0 = \begin{pmatrix} 0 & \mathbb{1}_{2\times 2} \\ \mathbb{1}_{2\times 2} & 0 \end{pmatrix}, \ \gamma^k = \begin{pmatrix} 0 & \sigma^k \\ -\sigma^k & 0 \end{pmatrix}, \ \gamma^5 = \begin{pmatrix} -\mathbb{1}_{2\times 2} & 0 \\ 0 & \mathbb{1}_{2\times 2} \end{pmatrix} \tag{A.3}$$

$$\gamma^0\gamma^k = \begin{pmatrix} -\sigma^k & 0 \\ 0 & \sigma^k \end{pmatrix}, \ \gamma^0\gamma^5 = \begin{pmatrix} 0 & \mathbb{1}_{2\times 2} \\ -\mathbb{1}_{2\times 2} & 0 \end{pmatrix} \tag{A.4}$$

with the Pauli matrices

$$\sigma^1 = \begin{pmatrix} 0 & 1 \\ 1 & 0 \end{pmatrix}, \ \sigma^2 = \begin{pmatrix} 0 & -i \\ i & 0 \end{pmatrix}, \ \sigma^3 = \begin{pmatrix} 1 & 0 \\ 0 & -1 \end{pmatrix}. \tag{A.5}$$

We define the projectors

$$P_\pm = \frac{1}{2}\left(1 \pm \gamma^5\right), \tag{A.6}$$

in the chiral representation they are given by

$$P_+ = \begin{pmatrix} 0 & 0 \\ 0 & \mathbb{1} \end{pmatrix}, \ P_- = \begin{pmatrix} \mathbb{1} & 0 \\ 0 & 0 \end{pmatrix}. \tag{A.7}$$

A.2. Boosted eigenvalues with vector condensate

In the following the boosting procedure of Dominik Nickel is derived by the use of the Hamiltonian. Ensuing, we show that it is not possible in the same way to separate the transverse momenta if vector fields are included.

At first, we consider the effective Hamiltonian with scalar fields $\phi_s(\mathbf{x})$:

$$H = -i\gamma^0\gamma^k\partial_k + \gamma^0\left[m - 2g_s\phi_s(\mathbf{x})\right] \equiv -i\gamma^0\gamma^k\partial_k + \gamma_0 M(\mathbf{x}). \tag{A.8}$$

Squaring above Hamiltonian yields

$$H^2 = -\boldsymbol{\nabla}^2 + i\gamma^k\partial_k M(\mathbf{x}) + M^2(\mathbf{x}). \tag{A.9}$$

Considering one-dimensional modulations $M(\mathbf{x}) = M(z)$ the derivative in H^2 – and therefore H^2 itself – can be decomposed into longitudinal and transversal components

$$H^2 = -\partial_z^2 - \boldsymbol{\nabla}_\perp^2 + i\gamma^3 M'(z) + M^2(z) \equiv H_0^2 - \boldsymbol{\nabla}_\perp^2 \tag{A.10}$$

where H_0 can be identified as the Hamiltonian in the rest-frame of $\mathbf{p}_\perp$. $\boldsymbol{\nabla}_\perp$ is interpreted as the nabla operator consisting of the partial derivatives in the perpendicular directions. Now let $\Psi_0(z)$ and λ be the eigenvectors and eigenvalues, respectively, at $\mathbf{p}_\perp = \mathbf{0}$ which satisfy the $1+1$ dimensional eigenvalue problem

$$H_0\Psi_0(z) = \lambda\Psi_0(z) \tag{A.11}$$

then for H_0^2 holds

$$H_0^2\Psi_0(z) = \lambda^2\Psi_0(z). \tag{A.12}$$

Equivalently for the full Hamiltonian H and eigenvectors $\Psi(\mathbf{x})$ holds

$$H\Psi(\mathbf{x}) = E\Psi(\mathbf{x}) \tag{A.13}$$
$$H^2\Psi(\mathbf{x}) = E^2\Psi(\mathbf{x}) \tag{A.14}$$

where E are the full $3+1$ dimensional eigenvalues. For the eigenvectors following separation approach is chosen:

$$\Psi(\mathbf{x}) = \Psi_0(z)e^{i\mathbf{p}_\perp\cdot\mathbf{x}_\perp}. \tag{A.15}$$

Applying the approach to equation (A.14) yields

$$H^2\Psi(\mathbf{x}) = \left(H_0^2 - \boldsymbol{\nabla}_\perp^2\right)\Psi_0(z)e^{i\mathbf{p}_\perp\cdot\mathbf{x}_\perp} \tag{A.16}$$
$$= \left(\lambda^2 + \mathbf{p}_\perp^2\right)\Psi_0(z)e^{i\mathbf{p}_\perp\cdot\mathbf{x}_\perp} \tag{A.17}$$
$$= \left(\lambda^2 + \mathbf{p}_\perp^2\right)\Psi(\mathbf{x}) \tag{A.18}$$
$$\implies E^2 = \lambda^2 + \mathbf{p}_\perp^2. \tag{A.19}$$

If vector fields are included, the Hamiltonian with one-dimensionally varying condensates reads

$$H = -i\gamma^0\gamma^k\partial_k + \gamma^0 M(z) + V(z). \tag{A.20}$$

Obviously, for $V(z) = \text{const.}$ the eigenvalues are just shifted by V. In that case, the boosting procedure can still be applied. But in the following, we will consider the general case of spatially depending vector condensates. The squared Hamiltonian reads:

$$H^2 = H_0^2 - \boldsymbol{\nabla}_\perp^2 - 2i\gamma^0\gamma^\perp V(z)\partial_\perp \equiv H_0^2 + H_\perp^2 \text{ with} \tag{A.21}$$

$$H_0^2 = -\partial_z^2 + i\gamma^3 M'(z) + M^2(z) - 2i\gamma^0\gamma^3 V(z)\partial_z - i\gamma^0\gamma^3 V'(z) + 2\gamma^0 M(z)V(z) + V^2(z) \tag{A.22}$$

where $\gamma^\perp$ and $\partial_\perp$ denote the γ^1- and γ^2- matrices and the partial derivatives in the perpendicular directions, respectively. To solve the eigenvalue problem one would analogously choose a separation approach such as:

$$\Psi(\mathbf{x}) = \Psi_0(z)\Phi(\mathbf{x}_\perp) \tag{A.23}$$

where

$$\left(H_0^2 + H_\perp^2\right)\Psi_0(z)\Phi(\mathbf{x}_\perp) = H_0^2\Psi_0(z)\Phi(\mathbf{x}_\perp) + \Psi_0(z)H_\perp^2\Phi(\mathbf{x}_\perp) = E^2\Psi_0(z)\Phi(\mathbf{x}_\perp) \tag{A.24}$$

is satisfied.

As it is common in quantum mechanics the further procedure would be

$$\frac{1}{\Psi_0(z)}H_0^2\Psi_0(z) + \frac{1}{\Phi(\mathbf{x}_\perp)}H_\perp^2\Phi(\mathbf{x}_\perp) \equiv \lambda^2 + \delta E_\lambda^2 = E^2 \tag{A.25}$$

where

$$H_0^2\Psi_0(z) = \lambda^2\Psi_0(z) \text{ and} \tag{A.26}$$

$$H_\perp^2\Phi(\mathbf{x}_\perp) = \delta E_\lambda^2\Phi(\mathbf{x}_\perp) \tag{A.27}$$

holds and derive δE_λ explicitly. But here, the eigenvectors exhibit Dirac structure due to the gamma-matrices so this method does not work unless it is possible somehow to decouple the system from the Dirac structure.

A.3. Asymptotic eigenvalues

One of the most time-demanding parts in the calculations is the diagonalization of the Hamiltonian matrix. By restricting the matrix size with a cut-off, artifacts are expected which can only be reduced by choosing very large cut-offs about $10\,\text{GeV}$. In order to choose smaller cut-offs and reach higher precision in the calculations, we will take advantage of the asymptotic behavior of the eigenvalues for large momenta parallel to the modulation. This can be done since $(k_z + rq)$ is expected to be much larger than M_i and $\tilde{\mu}_i$. The asymptotic behavior of the eigenvalues can be approximated by the homogeneous eigenvalues. Another approach could be using standard quantum mechanics perturbation methods, see [41] for further details, where the inhomogeneous condensates are respected. This has been done in [23]. But further

analyses show that approximating the full eigenvalues only with the homogeneous eigenvalues is more precise. To compare both methods the procedure of the perturbation method will be discussed briefly. The Hamiltonian can be divided into $H \approx H_0 + H_1$, with the unperturbed and perturbation part H_0 and H_1, respectively, which are given by

$$(H_0)_{p,p'} = \gamma^0\gamma^3(k_z - nq)\delta_{p,p'} + \gamma^0\gamma^1 p_\perp\delta_{p,p'} + \gamma^0 M_0\delta_{p,p'} \tag{A.28}$$

$$(H_1)_{p,p'} = \gamma^0 M_1\delta_{p,p'+q} + \gamma^0 M_1\delta_{p,p'-q} - \tilde{\mu}_1\delta_{p,p'-2q} - \tilde{\mu}_1\delta_{p,p'+2q} \tag{A.29}$$

H_0 is diagonal in momentum space so the eigenvalues can be calculated analytically

$$E_n^{(0)} = \pm\sqrt{(k_z - nq)^2 + M_0^2 + p_\perp^2}. \tag{A.30}$$

The corresponding eigenvectors $w_n^{(0)}$ of H_0 satisfy the relation

$$w_m^{(0)\dagger} w_n^{(0)} = \delta_{m,n}. \tag{A.31}$$

The perturbations up to second order are given by

$$E_n^{(1)} = w_n^{(0)\dagger} H_1 w_n^{(0)} \tag{A.32}$$

$$E_n^{(2)} = \sum_{m\neq n} \frac{\left|w_m^{(0)\dagger} H_1 w_n^{(0)}\right|^2}{E_n^{(0)} - E_m^{(0)}} \tag{A.33}$$

Since the eigenvectors are non-vanishing just if $p = p'$ it is obvious that $E_n^{(1)}$ vanish as it contains only off-diagonal entries in momentum space. In contrast $E_n^{(2)}$ contributes for the momenta which differ by the corresponding multiples of q. $E_n^{(2)}$ yields

$$E_n^{(2)} = \sum_{m\neq n} \frac{\left|M_1\delta_{m,n\mp 1} - \tilde{\mu}_1\delta_{m,n\mp 2}\right|^2}{E_n^{(0)} - E_m^{(0)}} \tag{A.34}$$

$$= \frac{M_1^2}{E_n^{(0)} - E_{n+1}^{(0)}} + \frac{M_1^2}{E_n^{(0)} - E_{n-1}^{(0)}} + \frac{\tilde{\mu}_1^2}{E_n^{(0)} - E_{n+2}^{(0)}} + \frac{\tilde{\mu}_1^2}{E_n^{(0)} - E_{n-2}^{(0)}} \tag{A.35}$$

Due to the Kronecker delta, there are no mixed terms from the square in equation (A.34). The energy correction up to second order is

$$E_\lambda^{(\infty)} \equiv E_\lambda^{(0)} + E_\lambda^{(2)}, \tag{A.36}$$

where, due to the degeneracy in Dirac space, each energy contributes two times. The relative differences between the exact eigenvalues E_λ and the energies from the perturbation ansatz $E_\lambda^{(\infty)}$ are plotted against E_λ in figure A.1 left. In the right picture of figure A.1 the same is plotted for E_λ and the unperturbed eigenvalues $E_\lambda^{(0)}$. To find a feasible cutoff for the matrix the approximated eigenvalues are compared to the exact ones using a large matrix cutoff Λ_M. The relative difference for the energy-corrected eigenvalues and for the unperturbed eigenvalues drops under $1\,‰$ at about $E_\lambda = 5\,\text{GeV}$ and $E_\lambda = 4\,\text{GeV}$, respectively. This shows that the approximation with the unperturbed eigenvalues is preferable. Furthermore, it leads to lesser computation times compared to using the corrected eigenvalues. This is true for all tested cases, so the matrix will be cut at $\Lambda_M = 6.5\,\text{GeV}$ to get even better precision and use the unperturbed eigenvalues for higher energies.
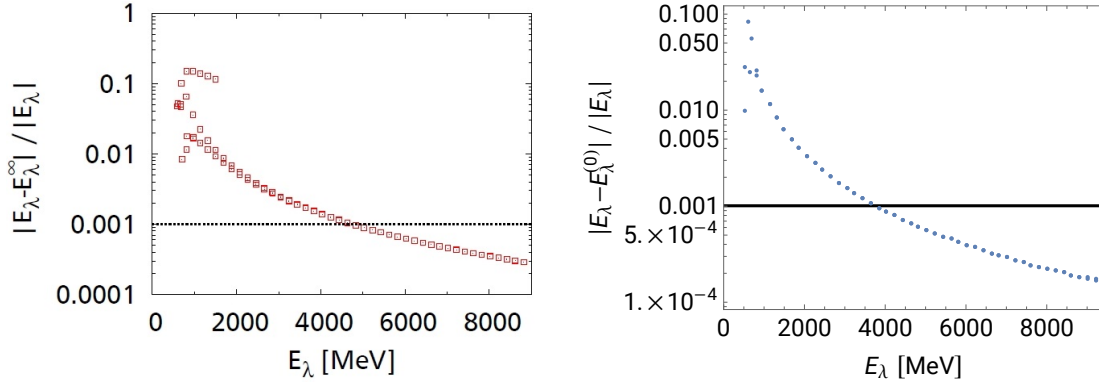
Figure A.1.: Relative difference between the exact eigenvalues of H and the energies from perturbation theory (left), taken from [23], and the eigenvalues of the unperturbed Hamiltonian H_0 (right). Both for exemplary values $k = 200\,\text{MeV}$, $p_\perp = 500\,\text{MeV}$, $q = 200\,\text{MeV}$, $M_0 = 0\,\text{MeV}$, $M_1 = 150\,\text{MeV}$ and $\tilde{\mu}_1 = 50\,\text{MeV}$. The matrix cutoff for H is $\Lambda_M = 10\,\text{GeV}$.

A.4. Asymptotic behavior of the integrand of Ω_{kin}

To further reduce the computation time, the asymptotic behavior of the integrand of Ω_{kin}

$$\omega_{\text{kin}} \equiv \sum_{j=0}^{3} c_j \left\{ \frac{E_{\lambda,j} - \text{sgn}(E_\lambda)\tilde{\mu}_0}{2} + (\tilde{\mu}_0 - E_{\lambda,j}) \cdot \Theta\left[\text{sgn}(E_\lambda)\tilde{\mu}_0 - E_{\lambda,j}\right] \right\} \tag{A.37}$$

for large energies is used. The result is a Laurent series where the relevant terms are given by

$$\omega_{\text{kin}} \longrightarrow \omega_{\text{kin}}^{\infty} \equiv E_\lambda \left[-\frac{3}{16}\left(\frac{\Lambda}{E_\lambda}\right)^6 + \frac{45}{64}\left(\frac{\Lambda}{E_\lambda}\right)^8 - \frac{525}{256}\left(\frac{\Lambda}{E_\lambda}\right)^{10} \right].$$

The relative difference between the exact integrand ω_{kin} and the asymptotic integrand $\omega_{\text{kin}}^{\infty}$ is plotted against E_λ in figure A.2. The relative difference drops under $0.01\,‰$ at about $E_\lambda = 9\,\text{GeV}$. This is true for all tested cases of μ. The asymptotic expression is used at energies $E_\lambda \geq 10\,\text{GeV}$ to get an even better precision.
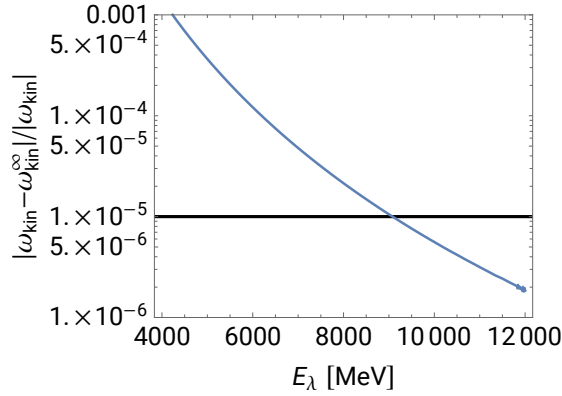
Figure A.2.: Relative difference between the exact integrand ω_{kin} and the asymptotic integrand $\omega_{\text{kin}}^{\infty}$ plotted against E_λ for $\mu = 360\,\text{MeV}$.

A.5. Simplifications of the kinetic part of the thermodynamic potential

In ADA, by using Nickel's boosting procedure, the perpendicular momenta can be excluded from the Hamiltonian matrix. So the matrix structure and equation (3.14) can further be simplified drastically. Doing so, the effective Hamiltonian in momentum space equation (4.2) reads

$$
H_{p_m,p_n} = \begin{pmatrix}
-(k+mq)\delta_{p_m,p_n} & 0 & \sum_{q_k} M_{q_k}\delta_{p_m,p_n+q} & 0 \\
0 & (k+mq)\delta_{p_m,p_n} & 0 & \sum_{q_k} M_{q_k}\delta_{p_m,p_n+q} \\
\sum_{q_k} M_{q_k}^*\delta_{p_m,p_n-q} & 0 & (k+mq)\delta_{p_m,p_n} & 0 \\
0 & \sum_{q_k} M_{q_k}^*\delta_{p_m,p_n-q} & 0 & -(k+mq)\delta_{p_m,p_n}
\end{pmatrix}
\tag{A.38}
$$

H_{p_m,p_n} contains of positive and negative eigenvalue pairs. This allows us to sum only over the positive eigenvalues. For positive eigenvalues, the Heaviside function is limited by the shifted chemical potential so the medium part does not need to be regularized which gives us

$$
\Omega_{\text{kin}} = -\frac{N_f N_c}{(2\pi)^2} \int\limits_0^q \mathrm{d}k_z \int\limits_0^\infty \mathrm{d}p_\perp\, p_\perp \sum_{E_\lambda>0} \left\{ \sum_{j=0}^3 c_j \sqrt{\lambda^2(k_z) + p_\perp^2 + j\Lambda^2} \right.
$$
$$
\left. + \left(\tilde{\mu}_0 - \sqrt{\lambda^2(k_z) + p_\perp^2} \right) \cdot \Theta\left[\tilde{\mu}_0 - \sqrt{\lambda^2(k_z) + p_\perp^2} \right] \right\}
\tag{A.39}
$$

By unitary transformation in Dirac space

$$
U = \frac{1}{2}\left[-\gamma_0 P_+ \left(\gamma^1 - i\gamma^2\right) + P_- \left(\gamma^1 + i\gamma^2\right) + \left(\gamma_0 P_- + P_+\right)\left(\mathbb{1} + \gamma^3\right) \right] = \begin{pmatrix} 0 & 0 & 0 & 1 \\ 1 & 0 & 0 & 0 \\ 0 & 0 & 1 & 0 \\ 0 & 1 & 0 & 0 \end{pmatrix}
\tag{A.40}
$$

the Hamiltonian can be recast into the form

$$\tilde{H}'_{p_m,p_n} = \begin{pmatrix} -(k+mq)\delta_{p_m,p_n} & \sum_{q_k} M_{q_k}\delta_{p_m,p_n+q} & 0 & 0 \\ \sum_{q_k} M^*_{q_k}\delta_{p_m,p_n-q} & (k+mq)\delta_{p_m,p_n} & 0 & 0 \\ 0 & 0 & (k+mq)\delta_{p_m,p_n} & \sum_{q_k} M^*_{q_k}\delta_{p_m,p_n-q} \\ 0 & 0 & \sum_{q_k} M_{q_k}\delta_{p_m,p_n+q} & -(k+mq)\delta_{p_m,p_n} \end{pmatrix} \tag{A.41}$$

which can be block diagonalized

$$H_{p_m,p_n} = U^\dagger \left(H^+_{p_m,p_n} \oplus H^-_{p_m,p_n} \right) U. \tag{A.42}$$

$H^\pm_{p_m,p_n}$ are the Bogoliubov-de Gennes (BdG) Hamiltonians

$$\tilde{H}^+_{p_m,p_n} = \begin{pmatrix} -(k+mq)\delta_{p_m,p_n} & \sum_{q_k} M_{q_k}\delta_{p_m,p_n+q} \\ \sum_{q_k} M^*_{q_k}\delta_{p_m,p_n-q} & (k+mq)\delta_{p_m,p_n} \end{pmatrix} \tag{A.43}$$

$$\tilde{H}^-_{p_m,p_n} = \begin{pmatrix} (k+mq)\delta_{p_m,p_n} & \sum_{q_k} M^*_{q_k}\delta_{p_m,p_n-q} \\ \sum_{q_k} M_{q_k}\delta_{p_m,p_n+q} & -(k+mq)\delta_{p_m,p_n} \end{pmatrix} \tag{A.44}$$

which contain the same absolute values of the eigenvalues, so only one of the two matrices needs to be considered. Therefore, we have to sum over all eigenvalues of $\tilde{H}^+_{p_m,p_n}$ and take the absolute value of them. This results in an additional factor of 2. In the following, we will denote the eigenvalues of H with λ_{BdG}. Now the Hamiltonian matrix has a simpler structure since there are fewer off-diagonals and the integration over the transversal momenta can be performed analytically:

$$\Omega_{\mathrm{kin}} = \frac{N_f N_c}{(2\pi)^2} \int_0^q \mathrm{d}k_z \sum_{|\lambda_{\mathrm{BdG}}|} \left\{ \sum_{j=0}^3 \frac{c_j}{3} \left(\lambda^2_{\mathrm{BdG}} + j\Lambda^2 \right) - \sum_{s\in\{-1,1\}} \frac{1}{6}\Theta\left[s\tilde{\mu}_0 - \lambda_{\mathrm{BdG}} \right] \cdot \left(s\tilde{\mu}_0 \left(\tilde{\mu}_0^2 - 3\lambda^2_{\mathrm{BdG}} \right) + 2\lambda^3_{\mathrm{BdG}} \right) \right\} \tag{A.45}$$

Bibliography

[1] L. Kumar, Mod. Phys. Lett. A **28**, (2013) 133003.

[2] B. Friman et al. (ed.) Lect. Notes Phys. **814**, (2011) 1-980.

[3] M. A. Stephanov, *QCD phase diagram: an overview*, PoS LAT2006:024, (2006), arXiv:hep-lat/0701002v1.

[4] P. Braun-Munzinger and J. Wambach, *The Phase Diagram of Strongly-Interacting Matter*, Rev. Mod. Phys. (2008), arXiv:0801.4256 [hep-ph].

[5] K. Fukushima, T. Hatsuda, *The phase diagram of dense QCD*, Rept. Prog. Phys. **74** (2011) 014001, arXiv:1005.4814 [hep-ph].

[6] M. Buballa, S. Carignano, *Inhomogeneous chiral condensates*, Prog. Part. Nucl. Phys. **81** (2014) 39–96, arXiv:1406.1367v2 [hep-ph].

[7] F. Karsch, *Lattice QCD at high temperature and density*, Lect. Notes Phys. **583** (2002) 209–249, arXiv:hep-lat/0106019.

[8] E. S. Swanson, *A Primer on Functional Methods and the Schwinger-Dyson Equations*, AIP Conf. Proc. **1296** (2010) 1, 75-121, arXiv:1008.4337v2 [hep-ph].

[9] E. Gutiérrez et. al, *The QCD phase diagram from Schwinger-Dyson Equations*, J. Phys. **41** (2014) 075002, arXiv:1304.8065v1 [hep-ph].

[10] C. S. Fischer, *QCD at finite temperature and chemical potential from Dyson-Schwinger equations*, Prog. Part. Nucl. Phys. **105**, 1 (2019), arXiv:1810.12938 [hep-ph].

[11] C. Wetterich, *Exact evolution equation for the effective potential*, Phys. Let. B **301** (1993) 90–94, arXiv:1710.05815v1 [hep-th].

[12] J. M. Pawlowski, *Aspects of the Functional Renormalisation Group*, Annals Phys. **322** (2007) 2831, arXiv:hep-th/0512261.

[13] J. M. Pawlowski, *Introduction to the functional RG and applications to gauge theories*, Lect. Notes Phys. **852** (2012) 287, arXiv:hep-ph/0512261.

[14] Y. Nambu, G. Jona-Lasinio, *Dynamical model of elementary particles based on an analogy with superconductivity*, i. Phys. Rev. **122** (1961) 345-358.

[15] Y. Nambu and G. Jona-Lasinio, *Dynamical model of elementary particles based on an analogy with superconductivity*, ii. Phys. Rev. **124** (1961) 246-254.

[16] M. Gell-Mann, M. Levy, *The axial vector current in beta decay*, Nuovo Cim. **16** (1960) 705.

[17] O. Scavenius, A. Mocsy, I.N. Mishustin, D.H. Rischke, *Chiral phase transition within effective models with constituent quarks*, Phys. Rev. C **64** (2001) 045202.

[18] URL: `https://www-alt.gsi.de/forschung/fair_experiments/CBM/Phasendiagram.jpg`.

[19] A. W. Overhauser, *Structure of Nuclear Matter*, Phys. Rev. **4** (1960) 415.

[20] P. Fulde, R. A. Ferrell, *Superconductivity in a strong spin-exchange field*, Phys. Rev. **135** (1964) A 550.

[21] A. I. Larkin, Y. N. Ovchinnikov, *Nonuniform state of superconductors*, Zh. Eksp. Teor. Fiz. **47** (1964) 1136.

[22] E. Alert, *Gap equations at inhomogeneous phases in the Nambu–Jona-Lasinio model*, Master's thesis, Institut für Kernphysik, Technische Universität Darmstadt, (2016). URL: `https://theorie.ikp.physik.tu-darmstadt.de/nhq/downloads/thesis/master.alert.pdf`.

[23] M. Schramm, *Inhomogeneous Phases in the Vector Interaction Extended Nambu–Jona-Lasinio Model*, Master's thesis, Institut für Kernphysik, Technische Universität Darmstadt, (2013). URL: `http://theorie.ikp.physik.tu-darmstadt.de/nhq/downloads/thesis/master.schramm.pdf`.

[24] S. Carignano, D. Nickel, and M. Buballa, *Influence of vector interaction and Polyakov loop dynamics on inhomogeneous chiral symmetry breaking phases*, Phys. Rev. D **82** (2010) 054009, arXiv:1007.1397 [hep-ph].

[25] D. Nickel, *Inhomogeneous phases in the Nambu-Jona–Lasino and quark-meson model*, Phys. Rev. D **80** (2009) 074025, arXiv:0906.5295 [hep-ph], MIT-CTP-4049.

[26] M. Thies, *Analytical solution of the Gross-Neveu model at finite density*, Phys.Rev. **D69** (2004) 067703, arXiv:hep-th/0308164v2.

[27] G. Basar, G. V. Dunne, *A Twisted Kink Crystal in the Chiral Gross-Neveu model*, Phys. Rev. **D78** (2008) 065022, arXiv:0806.2659v2 [hep-th].

[28] S. Carignano, M. Schramm, M. Buballa, *Influence of vector interactions on the favored shape of inhomogeneous chiral condensates*, Phys. Rev. D **98** (2018) 014033, arXiv:1805.06203v1 [hep-ph].

[29] M. Asakawa, K. Yazaki, *Chiral restoration at finite density and temperature*, Nuclear Phys. A **504** (1989) 668.

[30] S. Klevansky, *The Nambu-Jona-Lasinio model of quantum chromodynamics*, Rev. Mod. Phys. **64** (1992) 649–708.

[31] W. Pauli and F. Villars, *On the Invariant Regularization in Relativistic Quantum Theory*, Rev. Mod. Phys. **21** (1949) 434–444, URL: `http://link.aps.org/doi/10.1103/RevModPhys.21.434`.

[32] M. Buballa, *NJL-model analysis of dense quark matter*, Phys. Rept. **407** (2005) 205-376, arXiv:hep-ph/0402234v2.

[33] J. Gasser, H. Leutwyler, *Low energy theorems as precision tests of QCD*, Physics Letters B **125** no. 4 (1983) 325–329, URL: `http://www.sciencedirect.com/science/article/pii/0370269383912947`.

[34] T. D. Cohen, *Functional integrals for QCD at nonzero chemical potential and zero density*, Phys. Rev.Lett. **91** (2003) 222001, arXiv:hep-ph/0307089v4.

[35] F. Bloch, *Über die Quantenmechanik der Elektronen in Kristallgittern*, Z. Physik **52**, (1929) 555–600.

[36] C. Kittel, *Introduction to Solid State Physics*, Wiley John & Sons, (2004) 35.

[37] J. A. Nelder and R. Mead, *A Simplex Method for Function Minimization*, Computer Journal **7** (1965) 308-313.

[38] E. Anderson, Z. Bai, C. Bischof, S. Blackford, J. Demmel, J. Dongarra, J. Du Croz, A. Greenbaum, S. Hammarling, A. McKenney, D. Sorensen, *LAPACK Users' Guide. Society for Industrial and Applied Mathematics*, Philadelphia, PA, third edition, (1999).

[39] O. Schnetz, M. Thies, K. Urlichs, *Phase Diagram of the Gross-Neveu Model: Exact Results and Condensed Matter Precursors*, Ann. Physics **314** (2004) 425. arXiv:hep-th/0402014.

[40] O. Schnetz, M. Thies, K. Urlichs *Full Phase Diagram of the Massive Gross-Neveu Model*, Annals Phys. **321** (2006) 2604-2637, arXiv:hep-th/0511206v2.

[41] J. J. Sakurai, J. Napolitano, *Modern Quantum Mechanics*, Cambridge University Press, (2017) 306–310.